

GRAVITATIONAL ENCOUNTERS AND THE EVOLUTION OF GALACTIC NUCLEI. II. CLASSICAL AND RESONANT RELAXATION

DAVID MERRITT

Department of Physics and Center for Computational Relativity and Gravitation, Rochester Institute of Technology, Rochester, NY
 14623

Draft version July 24, 2018

ABSTRACT

Direct numerical integrations of the Fokker-Planck equation in energy-angular momentum space are carried out for stars orbiting a supermassive black hole (SBH) at the center of a galaxy. The algorithm, which was described in detail in an earlier paper, includes diffusion coefficients that describe the effects of both random (“classical”) and correlated (“resonant”) encounters. Steady-state solutions are similar to the Bahcall-Wolf solution, $n(r) \propto r^{-7/4}$, but are modified at small radii due to the higher rate of diffusion in angular momentum, which results in a low-density core. The core radius is a few percent of the influence radius of the SBH. The corresponding phase-space density $f(E, L)$ drops nearly to zero at low energies, implying almost no stars on tightly-bound orbits about the SBH. Steady-state rates of stellar disruption are presented, and a simple analytic expression is found that reproduces the numerical feeding rates with good accuracy. The distribution of periapsides of disrupted stars is also computed. Time-dependent solutions, $f(E, L, t)$, are also computed, starting from initial conditions similar to those produced by a binary SBH. In these models, feeding rates evolve on two timescales: rapid evolution during which the region evacuated by the massive binary is refilled by angular-momentum diffusion; and slower evolution as diffusion in energy causes the density profile at large radii to attain the Bahcall-Wolf form.

1. INTRODUCTION

Paper I in this series (Merritt 2015) presented a numerical algorithm for integrating the Fokker-Planck equation describing $f(E, L, t)$, the phase-space density of stars orbiting a SBH at the center of a galaxy. The algorithm described in Paper I was similar to that in the pioneering study of Cohn & Kulsrud (1978), but with a few modifications. Loss of stars into the SBH was treated more carefully, by adopting a logarithmic grid in angular momentum and by incorporating a more precise expression for the loss-cone flux. In addition, the diffusion coefficients in energy, E , and angular momentum, L , were allowed to have more general forms than those derived in the classical theory of Chandrasekhar, Hénon, Spitzer and others, all of whom assumed random (uncorrelated) interactions, and (with a few notable exceptions, e.g. Lee (1969)) ignored relativistic corrections to the equations of motion.

Two characteristic length scales are commonly associated with a supermassive black hole (SBH) at the center of a galaxy. The gravitational radius r_g ,

$$r_g \equiv \frac{GM_\bullet}{c^2} \approx 4.80 \times 10^{-8} \left(\frac{M_\bullet}{10^6 M_\odot} \right) \text{ pc}, \quad (1)$$

is the length scale set by Einstein’s equations for a relativistically compact object. The (gravitational) influence radius, r_{infl} , has two standard definitions: either $r_{\text{infl}} = r_h$, where

$$r_h \equiv \frac{GM_\bullet}{\sigma^2} = \left(\frac{c}{\sigma} \right)^2 r_g \approx 0.43 \left(\frac{M_\bullet}{10^6 M_\odot} \right) \left(\frac{\sigma}{100 \text{ km s}^{-1}} \right)^{-2} \text{ pc}; \quad (2)$$

or $r_{\text{infl}} = r_m$, defined implicitly via

$$M_\star(r < r_m) = 2M_\bullet. \quad (3)$$

The first of these is expressed in terms of σ , the one-dimensional velocity dispersion of stars in the galactic nucleus, while the second is defined as the radius containing a stellar (distributed) mass equal to twice M_\bullet . In the Milky Way, $r_h \approx r_m \approx 10^{0.5} \text{ pc}$ (Schödel et al. 2009; Chatzopoulos et al. 2015).

The classical theory of gravitational encounters is valid at distances $r \gtrsim r_m$ from a SBH. In this regime, random encounters imply a similar timescale for changes in both E and L : the “two-body” relaxation time T_r , given by

$$T_r = \frac{0.34\sigma^3}{G^2 m_\star \rho \ln \Lambda} \approx 1.2 \times 10^{10} \left(\frac{\sigma}{100 \text{ km s}^{-1}} \right)^3 \left(\frac{\rho}{10^5 M_\odot \text{ pc}^{-3}} \right)^{-1} \left(\frac{m_\star}{M_\odot} \right)^{-1} \left(\frac{\ln \Lambda}{15} \right)^{-1} \text{ yr}. \quad (4)$$

Here ρ is the stellar mass density, m_\star is the mass of a single star, and $\ln \Lambda$ is the Coulomb logarithm (Chandrasekhar 1942). In Figure 1, the region where equation (4) defines the timescale associated with gravitational encounters is labelled “Newton.”

If one imagines approaching ever more closely to the SBH, the unperturbed orbits change in well-defined ways, implying corresponding changes in the dominant mode of gravitational interaction between stars. Starting at a radius of $\sim 10^{-1}r_m$,¹ orbits are so nearly Keplerian that the assumption of uncorrelated encounters breaks down. This is the regime of “resonant relaxation” (Rauch & Tremaine 1996) in which changes in L can occur on much shorter timescales than changes in E . The corresponding spatial region is labelled “Kepler” in Figure 1.

Still closer to the SBH, the lowest-order effects of general relativity (GR) begin to make themselves felt. Orbits experience planar (apsidal) precession due to the 1st post-Newtonian (1PN) corrections to the equations of motion. One consequence is that the coherence time for the resonant interactions described above is determined by GR in this region. In addition, the most eccentric orbits at a given energy will precess due to GR at a higher rate than most other orbits of similar energy, causing the former to behave in qualitatively different ways than the latter in response to perturbations (Merritt et al. 2011). The region where gravitational encounters are strongly affected by these 1PN relativistic effects is labelled “Schwarzschild” in Figure 1; this region has an outer radius of $\sim 10^{-2}r_m$.

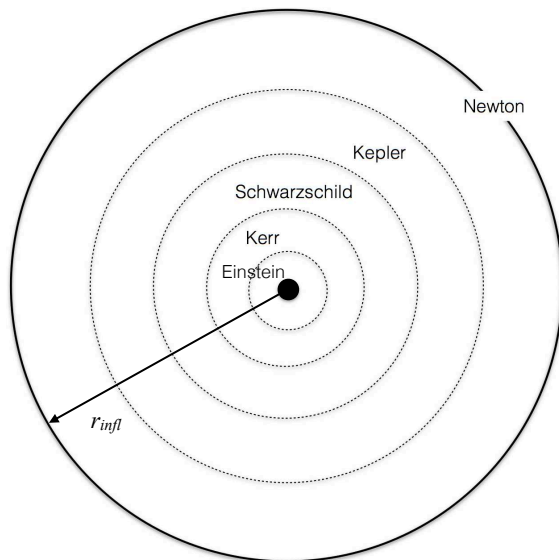


Fig. 1 – Sketch of the different regions around a massive black hole at the center of a spherical galaxy. Each region is defined in terms of the dominant mechanism by which gravitational encounters change the orbits of stars. The outer circle is the black hole’s gravitational influence radius r_{infl} and the inner circle is its gravitational radius r_g .

Another change in the character of the unperturbed motion occurs still closer to the SBH, where relativistic frame-dragging causes orbits to precess nodally about the spin axis of the SBH. While the importance of frame dragging for gravitational encounters has hardly begun to be explored, one consequence is known: within a certain distance, Lense-Thirring torques from a Kerr black hole dominate the Newtonian torques that would otherwise (via “vector resonant relaxation”) be responsible for changes in orbital planes (Merritt et al. 2010; Merritt & Vasiliev 2012). This region, of outer radius $\sim 10^{-3}r_m$, is labelled “Kerr” on Figure 1.

At still smaller radii, PN terms higher than 2nd order can become important, implying changes in E and L due to gravitational-wave emission. Within a distance of perhaps $10^2 r_g$ from the SBH, relativistic corrections can not be adequately treated via a Newtonian or post-Newtonian formalism. This regime is labelled “Einstein” in Figure 1. Of course the number of stars (or compact objects) present at any time in this region is likely to be small.

When evaluating the response of stellar orbits near a SBH to gravitational encounters, most researchers have applied the classical expressions for the diffusion coefficients, implicitly assuming that those expressions remain valid arbitrarily close to the SBH. An example is the Bahcall & Wolf (1976) steady-state solution for a single-component stellar cluster:

$$f \propto |E|^{1/4}, \quad n \propto r^{-7/4} \quad (5)$$

which was derived using the Hénon (1961) expressions for the orbit-averaged diffusion coefficients $\langle \Delta E \rangle$, $\langle (\Delta E)^2 \rangle$. This approach is defensible given that the form taken by the diffusion coefficients in the regions below “Newton” in Figure 1 can not yet be derived from first principles.

However, recent numerical work (Hamers, Portegies Zwart & Merritt 2014; Merritt 2015) has yielded approximate and fairly general expressions for the angular momentum diffusion coefficients in the “Kepler” regime. Those ex-

¹ More precise estimates of radii like this one are presented below.

pressions can be included in a Fokker-Planck description and used to evolve $f(E, L)$, yielding solutions that are valid—if not at all radii—at least to distances \sim ten times closer to the SBH than classical solutions like those of Bahcall & Wolf (1976) and Cohn & Kulsrud (1978). The diffusion coefficients adopted in the present paper are in fact valid even into the “Schwarzschild” regime of Figure 1, in the sense that they correctly account for the effects of 1PN apsidal precession on the coherence time. However, no attempt is made here to treat the effects of “anomalous relaxation,” the qualitatively different way in which low- L orbits evolve in the Schwarzschild regime (Merritt et al. 2011; Hamers, Portegies Zwart & Merritt 2014).

Section 2 reviews the numerical algorithm used here; further details are given in Paper I. In § 3, timescales associated with gravitational encounters in the “Newton,” “Kepler” and “Schwarzschild” regimes are derived for the case of stars in a Bahcall-Wolf cusp around a SBH. Section 4 presents steady-state and time-dependent solutions for $f(E, L)$. Section 5 discusses some implications of the results obtained here for real stellar systems and §6 sums up.

2. EVOLUTION EQUATIONS

The numerical algorithm for integrating the orbit-averaged Fokker-Planck equation is described in detail in Paper I. Features of the algorithm that are most relevant to the current study are reviewed here.

Stars are assumed to have a single mass, m_* , and to be close enough to the black hole (SBH) that the gravitational potential defining their unperturbed orbits is

$$\Phi(r) = -\frac{GM_\bullet}{r} \equiv -\psi(r) \quad (6)$$

with M_\bullet the SBH mass, assumed constant in time. Unperturbed orbits respect the two isolating integrals E , the energy per unit mass, and L , the angular momentum per unit mass. Following Cohn & Kulsrud (1978) these are replaced by \mathcal{E} and \mathcal{R} where

$$\mathcal{E} \equiv -E = -\frac{v^2}{2} + \psi(r), \quad \mathcal{R} \equiv \frac{L^2}{L_c^2}; \quad (7)$$

$L_c(\mathcal{E})$ is the angular momentum of a circular orbit of energy \mathcal{E} so that $0 \leq \mathcal{R} \leq 1$. \mathcal{E} and \mathcal{R} are related to the semimajor axis a and eccentricity e of the Kepler orbit via

$$a = \frac{GM_\bullet}{2\mathcal{E}}, \quad e^2 = 1 - \mathcal{R}. \quad (8)$$

The orbital (Kepler) period is

$$P = \frac{2\pi a^{3/2}}{\sqrt{GM_\bullet}} = \frac{\pi}{\sqrt{2}} \frac{GM_\bullet}{\mathcal{E}^{3/2}} \quad (9)$$

and $L_c = GM_\bullet/\sqrt{2\mathcal{E}} = \sqrt{GM_\bullet a}$. Spin of the SBH is ignored.

The time dependence of the phase-space number density of stars, $f(\mathcal{E}, \mathcal{R})$, is described by the orbit-averaged Fokker-Planck equation

$$\begin{aligned} \mathcal{J} \frac{\partial f}{\partial t} &= -\frac{\partial}{\partial \mathcal{E}} (\mathcal{J} \phi_{\mathcal{E}}) - \mathcal{J} \frac{\partial}{\partial \mathcal{R}} \phi_{\mathcal{R}}, \\ -\phi_{\mathcal{E}} &= D_{\mathcal{E}\mathcal{E}} \frac{\partial f}{\partial \mathcal{E}} + D_{\mathcal{E}\mathcal{R}} \frac{\partial f}{\partial \mathcal{R}} + D_{\mathcal{E}} f, \quad -\phi_{\mathcal{R}} = D_{\mathcal{R}\mathcal{E}} \frac{\partial f}{\partial \mathcal{E}} + D_{\mathcal{R}\mathcal{R}} \frac{\partial f}{\partial \mathcal{R}} + D_{\mathcal{R}} f \end{aligned} \quad (10)$$

with flux coefficients

$$\begin{aligned} D_{\mathcal{E}} &= -\langle \Delta \mathcal{E} \rangle - \frac{5}{4\mathcal{E}} \langle (\Delta \mathcal{E})^2 \rangle + \frac{1}{2} \frac{\partial}{\partial \mathcal{E}} \langle (\Delta \mathcal{E})^2 \rangle + \frac{1}{2} \frac{\partial}{\partial \mathcal{R}} \langle \Delta \mathcal{E} \Delta \mathcal{R} \rangle, \\ D_{\mathcal{R}} &= -\langle \Delta \mathcal{R} \rangle - \frac{5}{4\mathcal{E}} \langle \Delta \mathcal{E} \Delta \mathcal{R} \rangle + \frac{1}{2} \frac{\partial}{\partial \mathcal{E}} \langle \Delta \mathcal{E} \Delta \mathcal{R} \rangle + \frac{1}{2} \frac{\partial}{\partial \mathcal{R}} \langle (\Delta \mathcal{R})^2 \rangle, \\ D_{\mathcal{E}\mathcal{E}} &= \frac{1}{2} \langle (\Delta \mathcal{E})^2 \rangle, \quad D_{\mathcal{E}\mathcal{R}} = D_{\mathcal{R}\mathcal{E}} = \frac{1}{2} \langle \Delta \mathcal{E} \Delta \mathcal{R} \rangle, \quad D_{\mathcal{R}\mathcal{R}} = \frac{1}{2} \langle (\Delta \mathcal{R})^2 \rangle \end{aligned} \quad (11)$$

and $\mathcal{J} \equiv \sqrt{2}\pi^3 G^3 M_\bullet^3 \mathcal{E}^{-5/2}$ (Merritt 2013, 5.5.1). Quantities in $\langle \rangle$ are orbit-averaged diffusion coefficients, which are expressed as

$$\begin{aligned} \langle \Delta \mathcal{E} \rangle &= \langle \Delta \mathcal{E} \rangle_{\text{CK}}, \quad \langle (\Delta \mathcal{E})^2 \rangle = \langle (\Delta \mathcal{E})^2 \rangle_{\text{CK}}, \quad \langle \Delta \mathcal{E} \Delta \mathcal{R} \rangle = \langle \Delta \mathcal{E} \Delta \mathcal{R} \rangle_{\text{CK}}, \\ \langle \Delta \mathcal{R} \rangle &= \langle \Delta \mathcal{R} \rangle_{\text{CK}} + \langle \Delta \mathcal{R} \rangle_{\text{RR}}, \quad \langle (\Delta \mathcal{R})^2 \rangle = \langle (\Delta \mathcal{R})^2 \rangle_{\text{CK}} + \langle (\Delta \mathcal{R})^2 \rangle_{\text{RR}}. \end{aligned} \quad (12)$$

The subscript CK indicates that the diffusion coefficient is computed as in Cohn & Kulsrud (1978); their derivation was based on standard assumptions about randomness of encounters (Rosenbluth et al. 1957). The subscript RR refers to “resonant relaxation” (Rauch & Tremaine 1996). The resonant diffusion coefficients are assumed to have the simple, separable forms

$$\langle \Delta \mathcal{R} \rangle_{\text{RR}} = 2A(\mathcal{E})(1 - 2\mathcal{R}), \quad \langle (\Delta \mathcal{R})^2 \rangle_{\text{RR}} = 4A(\mathcal{E})\mathcal{R}(1 - \mathcal{R}). \quad (13)$$

The term containing the \mathcal{E} dependence is

$$A(a) = \alpha_s^2 \left[\frac{M_\star}{M_\bullet} \right]^2 \frac{1}{N} \frac{t_{\text{coh}}}{P^2}, \quad \alpha_s = 1.6, \quad a = \frac{GM_\bullet}{2\mathcal{E}}. \quad (14)$$

Here $N \equiv N(r < a)$ is the number of stars instantaneously at radii **smaller** than a , $M_\star = m_\star N$, P is the Kepler (radial) period, and t_{coh} is the coherence time, defined as

$$t_{\text{coh}}^{-1} \equiv t_{\text{coh,M}}^{-1} + t_{\text{coh,S}}^{-1} \\ t_{\text{coh,M}}(a) = \frac{M_\bullet}{Nm_\star} P, \quad t_{\text{coh,S}}(a) = \frac{1}{12} \frac{a}{r_g} P. \quad (15)$$

$t_{\text{coh,M}}$ is the mean precession time for stars of semimajor axis a due to the distributed mass around the SBH (“mass precession”), and $t_{\text{coh,S}}$ is the mean precession time due to the 1PN corrections to the Newtonian equations of motion (“Schwarzschild precession”).

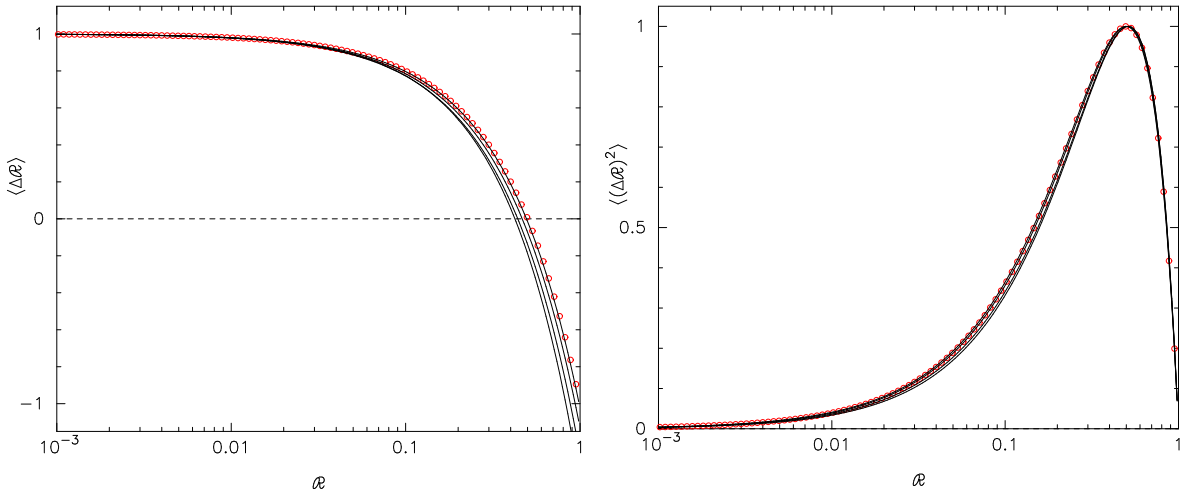


FIG. 2.— Angular momentum diffusion coefficients plotted as functions of $\mathcal{R} \equiv L^2/L_c^2$. Open (red) circles show equations (13), the adopted expressions for the resonant diffusion coefficients. Lines show the Cohn-Kulsrud diffusion coefficients, in models having $n(r) \propto r^{-\gamma}$, i.e. $f \propto \mathcal{E}^{\gamma-3/2}$, and $\gamma = \{1/2, 1, 3/2, 2\}$. Curves on the left are normalized to the same y -value at $\mathcal{R} = 0$, and curves on the right are normalized so as to have the same peak value. In the left panel, curves with largest γ have the smallest ordinate value at $\mathcal{R} = 1$; in the right panel, the curves with $\gamma = 0.5$ and $\gamma = 2$ have the largest ordinate values at $\mathcal{R} \approx 0.05$, while the two curves with $\gamma = 1$ and $\gamma = 3/2$ lie slightly below.

The functional forms chosen for the resonant diffusion coefficients in equations (13)-(15) were shown in Paper I to reproduce the numerically-extracted diffusion coefficients of Hamers, Portegies Zwart & Merritt (2014), at least in the particular set of scale-free nuclear models considered by those authors. Figure 2 makes another comparison: between the \mathcal{R} -dependence of the resonant diffusion coefficients, equations (13), and the \mathcal{R} -dependence of the classical diffusion coefficients. The latter were computed from equations (24)-(25) of Cohn & Kulsrud (1978), assuming scale-free forms for f and n :

$$f \propto \mathcal{E}^{\gamma-3/2}, \quad n \propto r^{-\gamma} \quad (16)$$

and a $1/r$ potential. The different curves in Figure 2 were normalized as described in the figure caption; of course the classical and resonant diffusion coefficients can have very different amplitudes. It is remarkable that the classical diffusion coefficients are very well fit by the same simple functions of \mathcal{R} that were adopted for the resonant diffusion coefficients; and furthermore that there is so little dependence of the former on γ . These results may lend an extra degree of confidence to the functional forms assumed here for the resonant diffusion coefficients.

Loss of stars into the SBH is controlled by the choice of r_{lc} , the radius of the physical loss sphere around the SBH, and by the conditions imposed on f at the loss-cone boundary, $\mathcal{R} = \mathcal{R}_{\text{lc}}(\mathcal{E})$, defined as

$$\mathcal{R}_{\text{lc}}(\mathcal{E}) = 2 \frac{\mathcal{E}}{\mathcal{E}_{\text{lc}}} \left(1 - \frac{1}{2} \frac{\mathcal{E}}{\mathcal{E}_{\text{lc}}} \right), \quad \mathcal{E} \leq \mathcal{E}_{\text{lc}}, \quad \mathcal{E}_{\text{lc}} \equiv \frac{GM_\bullet}{2r_{\text{lc}}}. \quad (17)$$

\mathcal{R}_{lc} is the normalized angular momentum of an orbit with (Newtonian) periapsis at r_{lc} . The \mathcal{R} -directed flux of stars across the loss-cone boundary is

$$F(\mathcal{E}) d\mathcal{E} = -\mathcal{J}(\mathcal{E}) \phi_{\mathcal{R}}(\mathcal{R}_{\text{lc}}) d\mathcal{E} \equiv -\mathcal{J}(\mathcal{E}) \phi_{\mathcal{R},\text{lc}}(\mathcal{E}) d\mathcal{E}. \quad (18)$$

Two quantities that play important roles in angular momentum diffusion near the loss-cone boundary are \mathcal{D} ,

$$\mathcal{D}(\mathcal{E}) \equiv \frac{\langle (\Delta \mathcal{R})^2 \rangle_t}{2\mathcal{R}} \Big|_{\mathcal{R}=\mathcal{R}_{lc}} = \frac{D_{\mathcal{R}\mathcal{R}}(\mathcal{E}, \mathcal{R}_{lc})}{\mathcal{R}_{lc}} \quad (19)$$

and q_{lc} ,

$$q_{lc}(\mathcal{E}) \equiv \frac{P(\mathcal{E})\mathcal{D}(\mathcal{E})}{\mathcal{R}_{lc}(\mathcal{E})}. \quad (20)$$

\mathcal{D}^{-1} is effectively an orbit-averaged, angular momentum relaxation time at energy \mathcal{E} . The quantity q_{lc} measures the change in angular momentum per orbital period, compared with the size of the loss cone. The loss-cone boundary conditions adopted in all the integrations presented here were the ‘‘Cohn-Kulsrud boundary conditions’’ defined in Paper I. No attempt is made to solve for f inside the loss cone, i.e. at $\mathcal{R} < \mathcal{R}_{lc}$, since f does not satisfy Jeans’s theorem in this region.

Solutions are obtained on a $(N_x \times N_z)$ grid in (X, Z) , where

$$\begin{aligned} X &\equiv \ln R = \ln \left[\frac{L}{L_c(\mathcal{E})} \right]^2, \\ Z &\equiv \ln(1 + \beta \mathcal{E}^*) = \ln(1 + \beta \mathcal{E}/c^2). \end{aligned} \quad (21)$$

Integrations presented here used $N_x = N_z = 64$ grid points.

The code adopts units such that

$$G = M_\bullet = c = 1 \quad (22)$$

allowing the results to be scaled to different masses of the SBH. Dimensionless parameters that must be specified before the start of an integration include m_\star/M_\bullet , $\ln \Lambda$ and $\Theta_{lc} \equiv r_{lc}/r_g$.

It is important to emphasize that all the results presented in this paper assume a single mass for the stars. One reason for this simplification is the current, poor state of knowledge about the form of the resonant diffusion coefficients in systems containing a range of stellar masses. The mass dependence of the classical diffusion coefficients is of course known; it implies a rate of energy loss for massive objects that scales in proportion to their mass, leading to segregation of the more massive objects toward the galaxy center. In steady-state models of the Milky Way nucleus that contain a realistic stellar mass function (Freitag et al. 2006; Hopman & Alexander 2006a), mass segregation implies that the total density is dominated by the heaviest stellar remnants, $\sim 10M_\odot$ black holes, inside a sphere of radius \sim a few $\times 10^{-3}$ pc.

3. IMPORTANT QUANTITIES IN A BAHCALL-WOLF CUSP

The steady-state numerical solutions presented later in this paper can be described as modifications of the classical Bahcall-Wolf solution, equation (5). Here we evaluate some important quantities associated with angular momentum diffusion in a nucleus with

$$\rho(r) \equiv m_\star n(r) \propto r^{-7/4}, \quad f(\mathcal{E}) \propto \mathcal{E}^{1/4}, \quad \psi(r) = \frac{GM_\bullet}{r}, \quad (23)$$

a unmodified Bahcall-Wolf (1976) cusp. Like Bahcall and Wolf, we ignore here the L -dependence that a realistic f would necessarily have due to capture by the hole.

Define r_m as the radius containing a mass in stars of $2M_\bullet$. The number density is

$$n(r) = n_0 \left(\frac{r}{r_0} \right)^{-7/4} = \frac{5}{8\pi} \frac{M_\bullet}{m_\star} \frac{1}{r_m^3} \left(\frac{r}{r_m} \right)^{-7/4}. \quad (24)$$

The number of stars with instantaneous radii less than r , or semimajor axes less than a , are given respectively by

$$N_r(< r) = 2 \frac{M_\bullet}{m_\star} \left(\frac{r}{r_m} \right)^{5/4}, \quad (25a)$$

$$N_a(< a) = \frac{\sqrt{\pi}}{2^{3/4}} \frac{\Gamma(11/4)}{\Gamma(5/4)} \frac{M_\bullet}{m_\star} \left(\frac{a}{r_m} \right)^{5/4} \approx 1.87 \frac{M_\bullet}{m_\star} \left(\frac{a}{r_m} \right)^{5/4}. \quad (25b)$$

The phase-space number density is

$$\begin{aligned} f(\mathcal{E}) &= \frac{5}{32} \sqrt{\frac{2}{\pi^5}} \frac{\Gamma(11/4)}{\Gamma(5/4)} \frac{M_\bullet}{m_\star} \frac{\mathcal{E}^{1/4}}{(GM_\bullet)^{7/4} r_m^{5/4}} = \frac{1}{4} \sqrt{\frac{2}{\pi^3}} \frac{\Gamma(11/4)}{\Gamma(5/4)} \frac{n_0 r_0^{7/4}}{(GM_\bullet)^{7/4}} \mathcal{E}^{1/4} \\ &\approx 0.022 \frac{M_\bullet}{m_\star} \frac{\mathcal{E}^{1/4}}{(GM_\bullet)^{7/4} r_m^{5/4}} \approx 0.11 \frac{n_0 r_0^{7/4} \mathcal{E}^{1/4}}{(GM_\bullet)^{7/4}} \end{aligned} \quad (26)$$

and the distribution of energies is

$$N(\mathcal{E}) d\mathcal{E} = 4\pi^2 p(\mathcal{E}) f(\mathcal{E}) d\mathcal{E}, \quad p(\mathcal{E}) = \frac{\sqrt{2}\pi}{4} (GM_\bullet)^3 \mathcal{E}^{-5/2}. \quad (27)$$

The mass coherence time, equation (15), is

$$t_{\text{coh},M}(a) = \frac{\pi r_m^{3/2}}{\sqrt{GM_\bullet}} \left(\frac{a}{r_m}\right)^{1/4} \approx 1.2 \times 10^5 \left(\frac{M_\bullet}{4 \times 10^6 M_\odot}\right)^{-1/2} \left(\frac{r_m}{3\text{pc}}\right)^{3/2} \left(\frac{a}{r_m}\right)^{1/4} \text{ yr} \quad (28)$$

and the Schwarzschild coherence time, equation (15b), is

$$t_{\text{coh},S}(a) = \frac{\pi}{6} \frac{c^2 a^{5/2}}{(GM_\bullet)^{3/2}} \approx 2.0 \times 10^{10} \left(\frac{M_\bullet}{4 \times 10^6 M_\odot}\right)^{-3/2} \left(\frac{a}{\text{pc}}\right)^{5/2} \text{ yr}. \quad (29)$$

These two times are equal when

$$a = 6^{4/9} (r_g^4 r_m^5)^{1/9} \quad (30)$$

or

$$\frac{a}{r_m} \approx 1.4 \times 10^{-3} \left(\frac{M_\bullet}{4 \times 10^6 M_\odot}\right)^{4/9} \left(\frac{r_m}{3\text{pc}}\right)^{-4/9}. \quad (31)$$

Figure 3 plots these times, as well as the coherence time $t_{\text{coh}}^{-1} \equiv t_{\text{coh},M}^{-1} + t_{\text{coh},S}^{-1}$ defined in equation (15):

$$t_{\text{coh}}(a) = \pi \sqrt{\frac{r_m^3}{GM_\bullet}} \left(\frac{a}{r_m}\right)^{1/4} \left(1 + \frac{6r_g r_m^{5/4}}{a^{9/4}}\right)^{-1} \quad (32)$$

assuming $M_\bullet = 4 \times 10^6 M_\odot$, and for two choices of r_m : 1 pc and 10 pc, which probably bracket the actual value at the Galactic center (Schödel et al. 2009; Chatzopoulos et al. 2015).

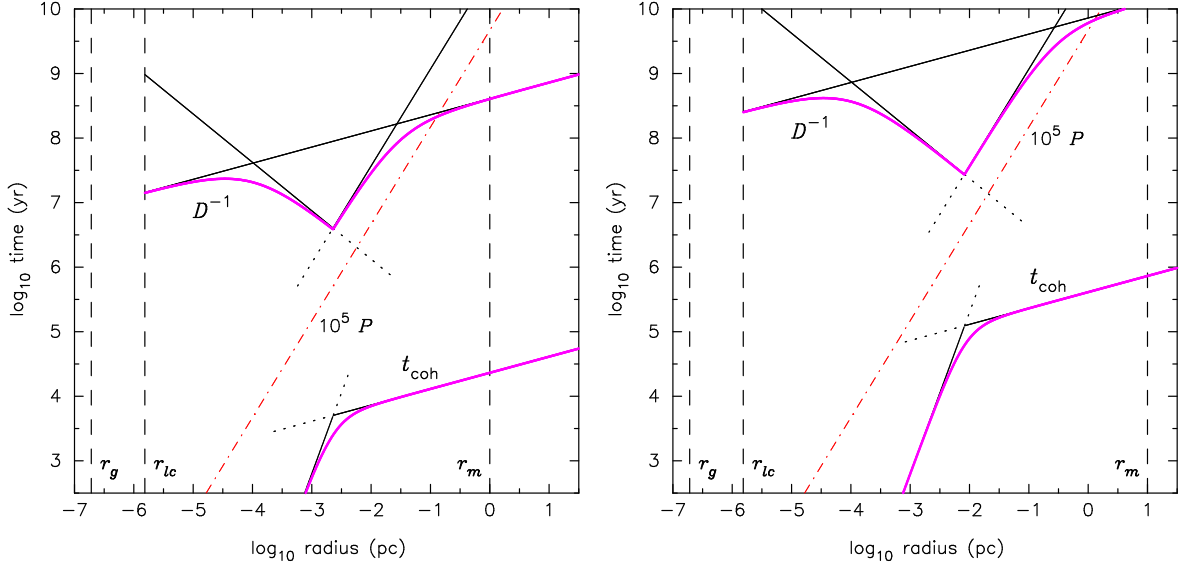


FIG. 3.— Characteristic times in a $n \propto r^{-7/4}$ nucleus. Parameters are $M_\bullet = 4 \times 10^6 M_\odot$, $m_\star = 1.0 M_\odot$, $r_m = 1$ pc (left) and $r_m = 10$ pc (right); the value of r_m at the Galactic center probably lies between these two values. The curve labelled r_{lc} assumes a capture radius of $8r_g$, appropriate for compact objects; tidal disruption of Solar-mass stars would occur at greater distances. The two solid (black) curves labelled t_{coh} show the coherence times due to mass- and Schwarzschild precession, equations (28) and (29) respectively; the mass (Schwarzschild) coherence time has the smaller (larger) value at large radii. Dot-dashed (red) line is 10^5 times the Kepler period P . Thick (magenta) curve shows the overall coherence time, equation (32). The three curves labelled D^{-1} are equations (34), (36), and (37); magenta curve is equation (39). In the case of the curves showing timescales, “radius” means “semimajor axis.”

The quantity \mathcal{D} defined in equation (19) is effectively an inverse, orbit-averaged, angular momentum relaxation time. In the case of classical relaxation, the CK diffusion coefficients imply, in the limit $\mathcal{R} \rightarrow 0$,

$$\mathcal{D}(\mathcal{E}) = 4\pi \Gamma C f(\mathcal{E}), \quad C = \frac{8}{385} \left[-158 + 45 \frac{\Gamma(1/4)}{\Gamma(3/4)} \sqrt{\pi} \right] \approx 1.62 \quad (33)$$

where $\Gamma \equiv 4\pi(Gm_*)^2 \ln \Lambda$, i.e.

$$\begin{aligned} \mathcal{D}(\mathcal{E}) &= \frac{5C}{\sqrt{2\pi}} \frac{\Gamma(11/4)}{\Gamma(5/4)} \frac{G^2 m_* M_\bullet \ln \Lambda}{(GM_\bullet)^{7/4} r_m^{5/4}} \mathcal{E}^{1/4}, \\ \mathcal{D}^{-1} &\approx 1.61 \times 10^9 \left(\frac{M_\bullet}{4 \times 10^6 M_\odot} \right)^{1/2} \left(\frac{r_m}{3 \text{ pc}} \right)^{5/4} \left(\frac{m_*}{M_\odot} \right)^{-1} \left(\frac{\ln \Lambda}{15} \right)^{-1} \left(\frac{a}{\text{pc}} \right)^{1/4} \text{ yr}. \end{aligned} \quad (34)$$

In the case that diffusion is dominated by resonant relaxation, equations (13) and (14) imply

$$\mathcal{D} = 2A = \frac{2\alpha_s^2 m_*}{\pi M_\bullet} \left(\frac{GM_\bullet}{r_m^3} \right)^{1/2} \frac{t_{\text{coh}}}{P} \left(\frac{a}{r_m} \right)^{-1/4}. \quad (35)$$

Setting $t_{\text{coh}} = t_{\text{coh,M}}$ gives

$$\begin{aligned} \mathcal{D} &= \frac{\alpha_s^2 m_*}{\pi M_\bullet} \sqrt{\frac{GM_\bullet}{a^3}}, \\ \mathcal{D}^{-1} &\approx 3.7 \times 10^{10} \left(\frac{M_\bullet/m_*}{4 \times 10^6} \right) \left(\frac{M_\bullet}{4 \times 10^6 M_\odot} \right)^{-1/2} \left(\frac{a}{\text{pc}} \right)^{3/2} \text{ yr} \end{aligned} \quad (36)$$

while setting $t_{\text{coh}} = t_{\text{coh,S}}$ gives

$$\begin{aligned} \mathcal{D} &= \frac{\alpha_s^2 m_*}{6\pi M_\bullet} \frac{c^2}{\sqrt{GM_\bullet r_m}} \left(\frac{a}{r_m} \right)^{3/4}, \\ \mathcal{D}^{-1} &\approx 1.66 \times 10^5 \left(\frac{M_\bullet/m_*}{4 \times 10^6} \right) \left(\frac{M_\bullet}{4 \times 10^6 M_\odot} \right)^{1/2} \left(\frac{r_m}{3 \text{ pc}} \right)^{5/4} \left(\frac{a}{\text{pc}} \right)^{-3/4} \text{ yr}. \end{aligned} \quad (37)$$

Equating (34) and (36) (which assumes $t_{\text{coh}} = t_{\text{coh,M}}$) yields an estimate of the radius below which resonant relaxation dominates classical relaxation:

$$\frac{a_{\text{eq}}}{r_m} \approx \frac{1}{2} \left[\frac{4\alpha_s^2}{5\sqrt{\pi}K} \frac{\Gamma(5/4)}{\Gamma(11/4)} \frac{1}{\ln \Lambda} \right]^{4/5} \approx 2.8 \times 10^{-2} \left(\frac{\ln \Lambda}{15} \right)^{-4/5}. \quad (38)$$

This radius can be identified with the sphere labelled ‘‘Kepler’’ in Figure 1.

Adopting equation (15) for the overall coherence time, we can write an expression that is valid throughout the resonant-relaxation-dominated regime:

$$\begin{aligned} \mathcal{D} &= \frac{\alpha_s^2 m_*}{\pi M_\bullet} \frac{\sqrt{GM_\bullet}}{a^{3/2}} \left(1 + \frac{6r_g r_m^{5/4}}{a^{9/4}} \right)^{-1}, \\ \mathcal{D}^{-1} &\approx 3.65 \times 10^{10} \left(\frac{M_\bullet/m_*}{4 \times 10^6} \right) \left(\frac{M_\bullet}{4 \times 10^6 M_\odot} \right)^{-1/2} \left(\frac{a}{\text{pc}} \right)^{3/2} \times \\ &\quad \left[1 + 4.55 \times 10^{-6} \left(\frac{M_\bullet}{4 \times 10^6 M_\odot} \right) \left(\frac{r_m}{3 \text{ pc}} \right)^{5/4} \left(\frac{a}{\text{pc}} \right)^{-9/4} \right] \text{ yr}. \end{aligned} \quad (39)$$

The diffusion time associated with resonant relaxation reaches a minimum when

$$a = 3^{4/9} (r_g^4 r_m^5)^{1/9} \quad (40)$$

slightly smaller than the radius at which $t_{\text{coh,M}} = t_{\text{coh,S}}$. Either of these radii can be associated with the sphere labelled ‘‘Schwarzschild’’ in Figure 1.

4. RESULTS

4.1. Steady-state solutions

Cohn & Kulsrud (1978) obtained various steady-state solutions for $f(\mathcal{E}, \mathcal{R})$, assuming classical relaxation, and with parameters chosen to represent stars orbiting a massive black hole in a globular cluster. As they noted, an algorithm that ignores the contribution of the distributed mass to the gravitational potential can not be expected to correctly represent the solution for f at low binding energies; that is, beyond the black hole’s gravitational influence radius. In all of their integrations, the outer boundary condition was taken to be

$$f(\mathcal{E} = 0, \mathcal{R}) = f_0 \quad (41)$$

and they identified f_0 with $n/(2\pi\langle v^2 \rangle)^{3/2}$; n and $\langle v^2 \rangle$ are respectively the number density and mean-square stellar velocity in the cluster core, where the density was assumed to be constant with radius. Cohn & Kulsrud interpreted their outer boundary condition as describing a fixed, Maxwellian velocity distribution at large distances from the black hole.

Solutions in this section were computed using a similar outer boundary condition:

$$f^*(\mathcal{E}_{\min}, \mathcal{R}, t) = f^*(\mathcal{E}_{\min}, \mathcal{R}, 0). \quad (42)$$

Here, f^* is the dimensionless phase-space density, and \mathcal{E}_{\min} is the minimum value of \mathcal{E} on the energy grid.² An approximately equivalent statement is that the outer boundary condition consisted of specifying a fixed mass density at the outermost grid radius.

Near the loss-cone boundary $\mathcal{R} = \mathcal{R}_{\text{lc}}(\mathcal{E})$, the Cohn-Kulsrud conditions were imposed, in the manner described in detail in Paper I.

The initial conditions for $f(\mathcal{E}, \mathcal{R})$ were based on an isotropic power-law model, $n \propto r^{-\gamma}$, $f \propto \mathcal{E}^{\gamma-3/2}$, but with a simple modification to account for the presence of the loss cone, namely

$$f(\mathcal{E}, \mathcal{R}) = 0, \quad \mathcal{R} \leq \mathcal{R}_{\text{lc}}(\mathcal{E}). \quad (43)$$

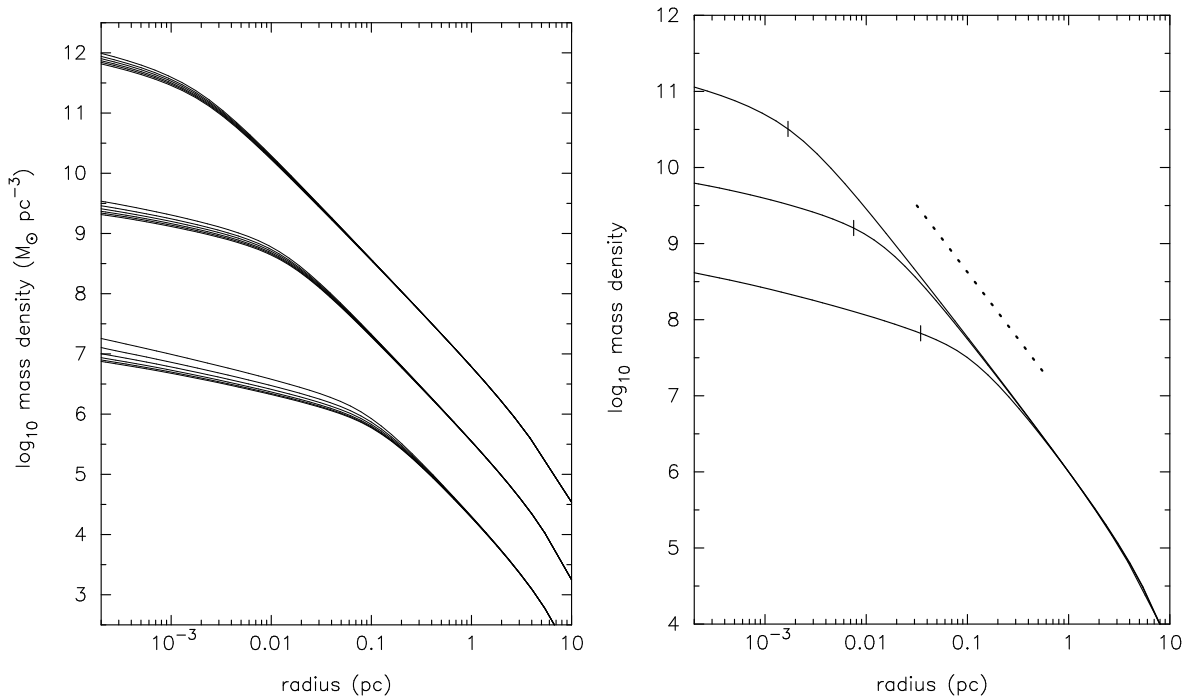


FIG. 4.— **Left panel:** Steady-state density profiles for integrations with three values of the outer density normalization and six values of m_*/M_\bullet . From bottom to top in each set, $m_* = \{0.3, 1, 3, 10, 30, 100\}M_\odot$, assuming $M_\bullet = 4.0 \times 10^6 M_\odot$. **Right panel:** The three curves from the left panel with $m_* = 1M_\odot$ have been replotted, and rescaled vertically to give the same mass density at $r = 1$ pc. Dotted line has the Bahcall-Wolf slope, $\rho \propto r^{-7/4}$. Vertical tick marks indicate where $t_{\text{coh},M} = t_{\text{coh},S}$.

Some examples showing the time-evolution of $n(r, t)$, starting from initial conditions similar to these, were presented in Paper I. Here we focus on the steady states. To minimize integration times, the value of γ defining the initial conditions was set to $7/4$, close to the expected, steady-state value. Integrations differed in their choice of two parameters: the outer mass density; and m_*/M_\bullet . Assuming $M_\bullet = 4 \times 10^6 M_\odot$ (the code sets the SBH mass to one), the adopted values of m_* were

$$m_* = \{0.3, 1, 3, 10, 30, 100\}M_\odot. \quad (44)$$

In principle, one could identify each value of m_* with stars of a certain type and estimate the corresponding tidal disruption radius. Instead, the radius r_{lc} of the loss sphere was chosen to be a fixed multiple of r_g in all integrations, $\Theta_{\text{lc}} \equiv r_{\text{lc}}/r_g = 15$, i.e.

$$r_{\text{lc}} = 15r_g \approx 2.9 \times 10^{-6} \left(\frac{M_\bullet}{4 \times 10^6 M_\odot} \right) \text{pc}, \quad (45)$$

roughly the value of the tidal-disruption radius for a Solar-type star at the Galactic center. Many properties of the steady-state solutions, including the rate of loss of stars to the SBH, are expected to depend only logarithmically on r_{lc} .

² It is likely that Cohn & Kulsrud also enforced their boundary condition at a finite \mathcal{E}_{\min} , and not at $\mathcal{E} = 0$.

Figure 4 shows steady-state density profiles for integrations with three different outer boundary conditions, corresponding to mass densities at one parsec of roughly

$$\{1.9 \times 10^4, 3.5 \times 10^5, 6.1 \times 10^6\} M_\odot \text{pc}^{-3}. \quad (46)$$

These values probably bracket the actual value in the Milky Way (Schödel et al. 2009; Chatzopoulos et al. 2015). The left panel shows solutions for each of the 18 models, i.e., six values of m_* for each choice of outer density. To a good approximation, the form of $\rho(r)$ is determined by the (mass) density normalization, independent of m_* . The reason can be seen by comparing equations (34), (36) and (37), which show that the rate of angular momentum diffusion scales with m_* in the same way for both classical and resonant relaxation, if a fixed value of r_m —that is, a fixed mass density—is assumed. The (weak) dependence of the steady-state density profile on m_* is due to the fact that q_{lc} , defined in equation (20), is also proportional to m_* . Solutions with the smallest m_* approach most closely to the “empty-loss-cone” form, $q_{lc} \ll 1$, for which

$$f(\mathcal{E}, \mathcal{R}) \approx f(\mathcal{E}, 1) \frac{\ln(\mathcal{R}/\mathcal{R}_{lc})}{\ln(1/\mathcal{R}_{lc})}, \quad \mathcal{R}_{lc}(\mathcal{E}) \leq \mathcal{R} \leq 1 \quad (47)$$

while large values of m_* imply $q_{lc} \gg 1$ and

$$f(\mathcal{E}, \mathcal{R}) \approx \text{const.}, \quad \mathcal{R}_{lc}(\mathcal{E}) \leq \mathcal{R} \leq 1, \quad (48)$$

the “full-loss-cone” solution (Merritt 2013, 6.1.2).

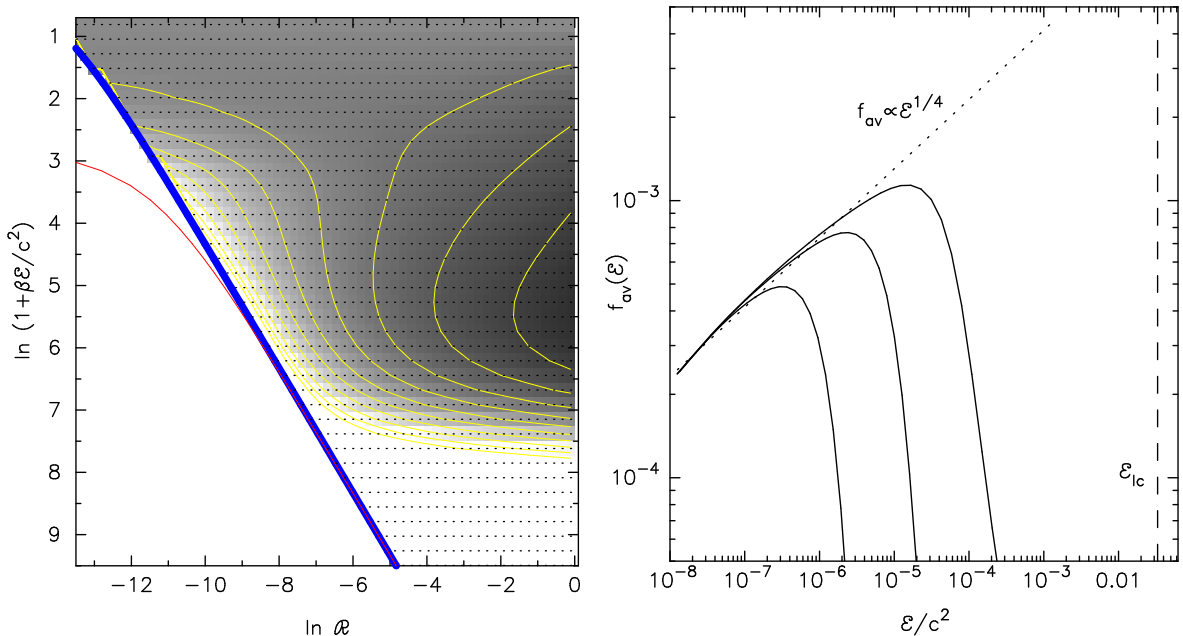


FIG. 5.— **Left:** Equilibrium phase-space density in the integration from Figure 4 with $m_*/M_\odot = 1$ and with a final density at 1 pc of $\sim 3.5 \times 10^5 M_\odot \text{pc}^{-3}$. Greyscale is proportional to $\log f$ and the thin (yellow) curves are contours of constant f . Thick (blue) curve is the loss-cone boundary and thin (red) curve is $\mathcal{R}_0(\mathcal{E})$. The solution grid was uniform in the plotted variables $\{X = \ln \mathcal{R}, Y = \ln(1 + \beta\mathcal{E}/c^2)\}$; grid centers are indicated with the dots. **Right:** Angular-momentum-averaged distribution functions for the three, steady-state models from Figure 4 with $m_* = M_\odot$; the middle curve corresponds to the steady-state f plotted at left. The vertical normalization of each curve was chosen to give a fixed value at low energies. Dotted line shows the Bahcall-Wolf solution and vertical dashed line indicates the energy of a circular orbit at the assumed radius of the capture sphere around the SBH.

Formation of a “core” is an expected consequence of resonant relaxation (Hopman & Alexander 2006b; Madigan et al. 2011). In the “Kepler” regime (Figure 1), diffusion in angular momentum takes place on a short timescale compared with diffusion in energy. As a consequence, stars in this region are scattered into the SBH in a time short compared with the time for the same orbits to be repopulated by (classical) energy diffusion. An estimate of the value of a below which resonant relaxation dominates classical relaxation was made in equation (38): $a \approx 3 \times 10^{-2} r_m$. Since

$$r_m \approx \{0.2, 2.0, 20\} \text{pc} \quad (49)$$

in the models of Figure 4, the value of a at transition is predicted to be $\sim \{6 \times 10^{-3}, 6 \times 10^{-2}, 6 \times 10^{-1}\}$ pc. It is reasonable to divide these values by ~ 2 to convert from a to radii. The resulting values are quite similar to the radii of the cores in Figure 4.

The right panel of Figure 4 compares the steady-state density profiles in the three integrations with $m_* = M_\odot$. To assist in the comparison, the curves have been adjusted vertically so as to have the same density at a radius of one parsec.

Depletion of f at high binding energies should eventually result in gradients with respect to E that drive a (classical) flux that balances the losses due to (resonant) diffusion in L . The left panels of Figures 5 and 6 provide support for this statement. Plotted there are the steady-state $f(\mathcal{E}, \mathcal{R})$ (Figure 5), and streamlines of the flow in $(\mathcal{E}, \mathcal{R})$ space (Figure 6), of the model from Figure 4 with $m_*/M_\odot = 1$ and with the intermediate, large-radius density. There is a remarkably strong depletion of f above a certain binding energy. The right panel of Figure 5 shows angular-momentum-averaged f 's:

$$\bar{f}(\mathcal{E}) = \int_0^1 f(\mathcal{E}, \mathcal{R}) d\mathcal{R} \quad (50)$$

for the three steady-state models from Figure 4 with $m_*/M_\odot = 1$. To a good approximation, $f = 0$ above a certain \mathcal{E} , and so the configuration-space density at small radii has the form

$$n(r) \sim r^{-1/2}, \quad (51)$$

the density of a population of stars with a single energy moving in a $1/r$ potential. This is approximately the central dependence of ρ on r in the profiles of Figure 4.

The thin (red) curve in the left panels of Figures 5 and 6 is the quantity $\mathcal{R}_0(\mathcal{E})$, the $f = 0$ intercept of the Cohn-Kulsrud boundary-layer solution extrapolated inside the loss cone (Merritt 2013, equation 6.65). An “empty” loss cone has $\mathcal{R}_0 \approx \mathcal{R}_{lc}$. At low binding energies, \mathcal{R}_0 can be seen to drop below \mathcal{R}_{lc} , indicating that the loss cone is becoming progressively fuller far from the SBH.

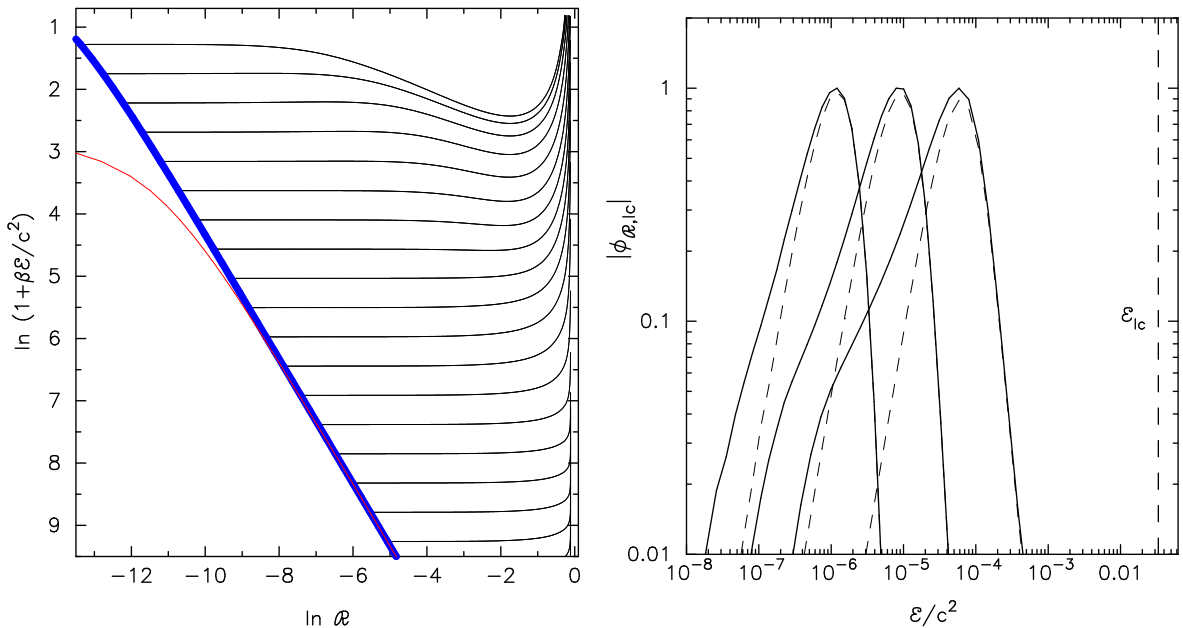


FIG. 6.— **Left:** Streamlines of the flux (equation 10) in the steady-state model of Figure 5. **Right:** Flux of stars into the loss cone as a function of energy. The three sets of curves correspond to the three models from Figure 4. Each curve has been normalized vertically to give a peak flux of one. Dashed curves show the contribution to $\phi_{\mathcal{R}}$ from resonant relaxation.

The right panel of Figure 6 plots the \mathcal{R} -directed flux, $\phi_{\mathcal{R}}$, at the loss-cone boundary as a function of energy, in the three steady-state models of Figure 4. Corresponding to the depletion of f at large binding energies, there is a similar depletion in the loss-cone flux, such that $\phi_{\mathcal{R}}$ peaks narrowly around a certain energy. The dashed curves in this figure show the contribution to the flux from resonant relaxation. As expected, the resonant contribution to the flux becomes dominant at roughly the same energy where the depletion in f occurs.

A quantity more directly related to the loss rate than $\phi_{\mathcal{R},lc}(\mathcal{E})$ is $F(\mathcal{E}) = -\mathcal{J}(\mathcal{E})\phi_{\mathcal{R},lc}(\mathcal{E})$; equation (18) states that the integral of $F(\mathcal{E})$ with respect to energy yields \dot{N} . The left panel of Figure 7 plots $|\mathcal{E}F(\mathcal{E})|$ for each of the 18 steady-state models of Figure 4. This quantity can be interpreted as the contribution to the total loss rate from stars in the energy interval $d\mathcal{E}/\mathcal{E}$, or equivalently, da/a . It is clear from this figure that there is a substantial contribution to the feeding rate from stars at large radii, hence in the classical regime, particularly in the case of small m_* , i.e. an empty loss cone. As m_* is increased (at fixed ρ), the radius of transition from full- to empty loss cones drops; the curves peak, roughly, at this radius. In the empty-loss-cone regime, near the SBH, loss rates (measured in stars per year) are nearly independent of m_* . This follows from the dependence $\mathcal{D} \sim m_*$, noted above, and the fact that for a fixed mass density, the number of stars scales as m_*^{-1} . Far from the SBH, in the full-loss-cone regime, the expressions derived below imply

$$|\phi_{\mathcal{R},lc}| \propto m_*^{-1} \mathcal{E}^{11/4}, \quad |\mathcal{E}F(\mathcal{E})| \propto m_*^{-1} \mathcal{E}^{5/4}, \quad \mathcal{E} \rightarrow 0. \quad (52)$$

The total loss rate diverges in the case of an everywhere-empty loss cone, $m_\star \rightarrow 0$, but is finite for finite m_\star .

The right panel of Figure 7 shows integrated loss rates for the same set of models. As expected, \dot{N} attains a well-defined limit at low \mathcal{E} , i.e. large a , in each model. These values are listed in Table 1, and plotted against m_\star in Figure 8. In three of the models, the adopted energy grid probably did not extend to low enough values of \mathcal{E} to yield accurate values for the total loss rate; these numbers have been placed in parentheses in Table 1.

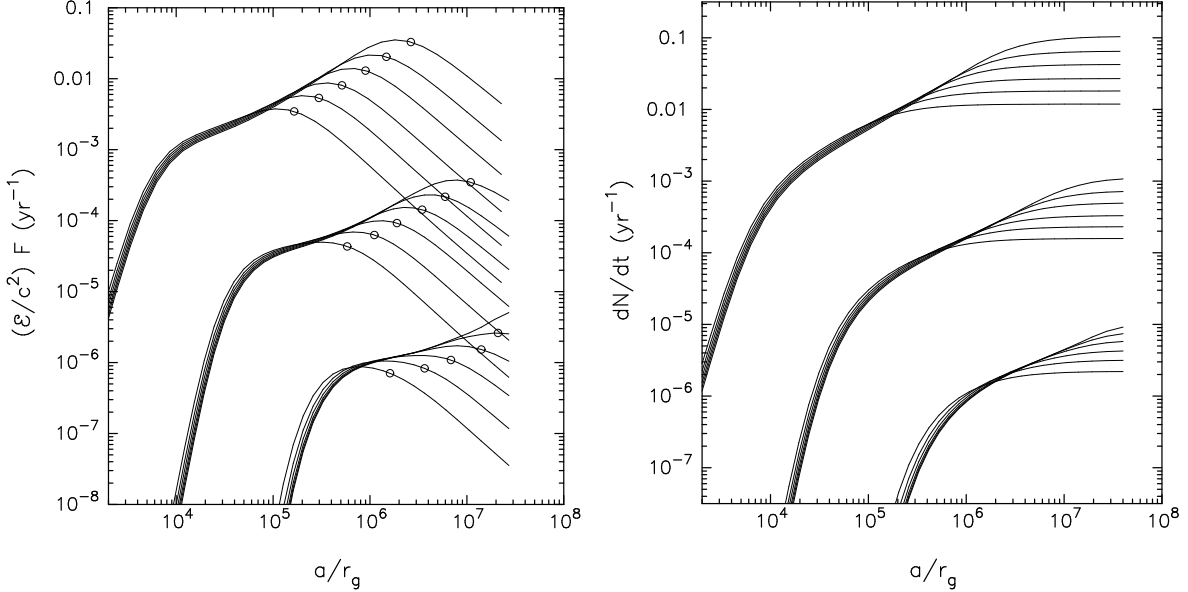


FIG. 7.— Local (left) and integrated (right) loss rates, defined as number of stars per year, for the equilibrium models of Figure 4, assuming $M_\bullet = 4 \times 10^6 M_\odot$. In each set of curves, the value of m_\star increases from top to bottom. The energy $\mathcal{E} = GM_\bullet/(2a)$ at which $q_{lc} = |\ln \mathcal{R}_{lc}|$ is indicated by a circle in the curves on the left.

It is useful to have an approximate analytic expression for the loss rate. Since most of the stars lost to the SBH are orbiting in the “Newton” regime prior to capture (Figure 7), it is reasonable to adopt the classical expressions for the angular-momentum diffusion coefficients at all energies. We simplify the derivation even more by (i) adopting for the density profile a Bahcall-Wolf cusp, unmodified by resonant relaxation and by loss-cone effects; and (ii) assuming that stars at any given energy are either in the empty-loss-cone, or the full-loss-cone, regimes at the time of capture. In the full-loss-cone (FLC) regime, f is assumed to be independent of \mathcal{R} , $f^{\text{FLC}}(\mathcal{E}, \mathcal{R}) = f(\mathcal{E})$. In the empty-loss-cone (ELC) regime, equation (47) for f can be written

$$f(\mathcal{R}; \mathcal{E}) \approx \frac{f(\mathcal{E}, 1)}{\ln(1/\mathcal{R}_{lc})} \ln\left(\frac{\mathcal{R}}{\mathcal{R}_{lc}}\right) \approx \frac{\bar{f}(\mathcal{E})}{\ln(1/\mathcal{R}_{lc}) + \mathcal{R}_{lc} - 1} \ln\left(\frac{\mathcal{R}}{\mathcal{R}_{lc}}\right), \quad \mathcal{R}_{lc} \leq \mathcal{R} \leq 1 \quad (53)$$

with $\bar{f}(\mathcal{E})$ defined as in equation (50). The differential loss rate, $F(\mathcal{E})$, is defined such that the number of stars lost, per unit of time, from orbits with energies in the range \mathcal{E} to $\mathcal{E} + d\mathcal{E}$ is $F(\mathcal{E})d\mathcal{E}$. In the FLC regime, the loss rate is equal to the orbital draining rate:

$$F^{\text{FLC}}(\mathcal{E}) = 4\pi^2 L_c^2(\mathcal{E}) \mathcal{R}_{lc}(\mathcal{E}) f(\mathcal{E}) = P(\mathcal{E})^{-1} \mathcal{R}_{lc}(\mathcal{E}) N(\mathcal{E}) \quad (54)$$

(Merritt 2013, equations (6.10,6.72)). The loss rate from stars in the ELC regime is

$$F^{\text{ELC}}(\mathcal{E}) = \frac{4\pi^2 L_c^2(\mathcal{E}) P(\mathcal{E}) \mathcal{D}(\mathcal{E})}{\ln(1/\mathcal{R}_{lc}) - 1 + \mathcal{R}_{lc}} \bar{f}(\mathcal{E}) = \frac{\mathcal{D}(\mathcal{E}) \bar{N}(\mathcal{E})}{\ln(1/\mathcal{R}_{lc}) - 1 + \mathcal{R}_{lc}} \approx \frac{\mathcal{D}(\mathcal{E}) \bar{N}(\mathcal{E})}{|\ln \mathcal{R}_{lc}|} \quad (55)$$

(Merritt 2013, equations (6.59)-(6.62)), i.e.

$$F^{\text{ELC}}(\mathcal{E}) \approx \frac{q_{lc}(\mathcal{E})}{|\ln \mathcal{R}_{lc}|} F^{\text{FLC}}(\mathcal{E}). \quad (56)$$

We assume that equation (54) describes $F(\mathcal{E})$ for $\mathcal{E} < \mathcal{E}_{\text{crit}}$ and that equation (55) describes $F(\mathcal{E})$ for $\mathcal{E} > \mathcal{E}_{\text{crit}}$, where $\mathcal{E}_{\text{crit}}$ is the energy separating the full- and empty-loss-cone regimes. Identifying $\bar{f}(\mathcal{E})$, $\bar{N}(\mathcal{E})$ and $\mathcal{D}(\mathcal{E})$ with the expressions for an unmodified Bahcall-Wolf cusp, as given in §3, the total loss rates from the two regimes can be

written in terms of $\mathcal{E}_{\text{crit}}$ after integration over \mathcal{E} , as:

$$\dot{N}^{FLC} \approx \sqrt{\frac{2}{\pi}} \frac{\Gamma(11/4)}{\Gamma(5/4)} \frac{M_{\bullet}}{m_{\star}} \frac{(GM_{\bullet})^{3/2}}{c^2 r_m^{5/2}} \frac{r_{\text{lc}}}{r_g} \left(\frac{\mathcal{E}_{\text{crit}}}{\mathcal{E}_m} \right)^{5/4}, \quad (57a)$$

$$\dot{N}^{ELC} \approx \frac{25\sqrt{2}}{32} C \left[\frac{\Gamma(11/4)}{\Gamma(5/4)} \right]^2 \frac{\ln \Lambda}{\ln \mathcal{R}_{\text{lc}}^{-1}} \sqrt{\frac{GM_{\bullet}}{r_m^3}} \left(\frac{\mathcal{E}_{\text{crit}}}{\mathcal{E}_m} \right)^{-1}, \quad \mathcal{E}_m \equiv \frac{GM_{\bullet}}{r_m}. \quad (57b)$$

The constant $C \approx 1.62$ is defined in equation (33). In the integral for \dot{N}^{ELC} , the term $\ln \mathcal{R}_{\text{lc}}$ was assumed independent of \mathcal{E} ; a reasonable choice for this term might be its value at $\mathcal{E} = \mathcal{E}_{\text{crit}}$, i.e. $\ln \mathcal{R}(\mathcal{E}_{\text{crit}})$.

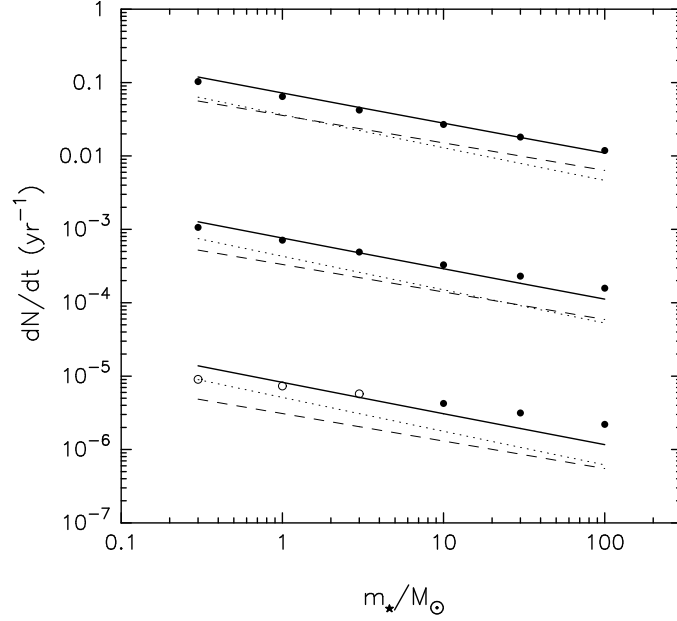


FIG. 8.— Loss rates for the models of Figure 7. Scaling assumes $M_{\bullet} = 4 \times 10^6 M_{\odot}$. Plotted points are the same numbers given in Table 1; dashed and dotted curves are the approximate analytic relations derived in the text for the full- and empty-loss-cone regimes respectively, and their sum is shown as the solid curves. The open circles are from numerical integrations in which the \mathcal{E} -grid probably did not extend to low enough values to yield the correct, total loss rates (see the right panel of Figure 7).

TABLE 1
STEADY-STATE LOSS RATES

ρ ($r = 1$ pc) ($M_{\odot} \text{pc}^{-3}$)	m_{\star}/M_{\odot}	\dot{N} (yr^{-1}) (numerical)	$\dot{N}^{\text{ELC}}/\dot{N}$ (analytic)
1.9×10^4	0.3	(9.03×10^{-6})	0.65
	1.0	(7.34×10^{-6})	0.62
	3.0	(5.74×10^{-6})	0.60
	10.	4.24×10^{-6}	0.58
	30.	3.14×10^{-6}	0.55
	100.	2.20×10^{-6}	0.53
3.5×10^5	0.3	1.06×10^{-3}	0.59
	1.0	7.12×10^{-4}	0.56
	3.0	4.91×10^{-4}	0.54
	10.	3.29×10^{-4}	0.52
	30.	2.31×10^{-4}	0.50
	100.	1.58×10^{-4}	0.47
6.1×10^6	0.3	1.03×10^{-1}	0.53
	1.0	6.45×10^{-2}	0.51
	3.0	4.22×10^{-2}	0.48
	10.	2.69×10^{-2}	0.46
	30.	1.81×10^{-2}	0.44
	100.	1.18×10^{-2}	0.42

We take for $\mathcal{E}_{\text{crit}}$ the energy that satisfies

$$q_{\text{lc}}(\mathcal{E}_{\text{crit}}) = |\ln \mathcal{R}_{\text{lc}}| \quad (58)$$

since at this energy, equation (56) suggests that $F^{\text{ELC}} \approx F^{\text{FLC}}$. Using equations (9), (20) and (34) we find

$$q_{\text{lc}}(\mathcal{E}) = q_0 \left(\frac{\mathcal{E}}{\mathcal{E}_m} \right)^{-5/4} \frac{m_\star}{M_\bullet} \frac{\ln \Lambda}{\mathcal{R}_{\text{lc}}(\mathcal{E})}, \quad q_0 \equiv \frac{5\sqrt{\pi}}{2} \frac{\Gamma(11/4)}{\Gamma(5/4)} C \approx 12.73.$$

When solving for $\mathcal{E}_{\text{crit}} \ll \mathcal{E}_{\text{lc}}$, the expression for q_{lc} can be simplified by writing $\mathcal{R}_{\text{lc}}(\mathcal{E}) \approx 2\mathcal{E}/\mathcal{E}_{\text{lc}}$, or

$$q(\mathcal{E}_{\text{crit}}) \approx \frac{q_0}{2} \frac{m_\star}{M_\bullet} \ln \Lambda \frac{\mathcal{E}_{\text{lc}}}{\mathcal{E}_m} \left(\frac{\mathcal{E}_{\text{crit}}}{\mathcal{E}_m} \right)^{-9/4}. \quad (59)$$

Equating this with $-\ln \mathcal{R}_{\text{lc}}$ yields a transcendental equation for $x \equiv \mathcal{E}_{\text{crit}}/\mathcal{E}_{\text{lc}}$:

$$x^{9/4} \ln(2x) = -\frac{q_0}{2} \frac{m_\star}{M_\bullet} \ln \Lambda \left(\frac{\mathcal{E}_m}{\mathcal{E}_{\text{lc}}} \right)^{5/4}. \quad (60)$$

For values of x in the range of interest ($10^{-7} \lesssim x \lesssim 10^{-5}$), an approximate solution to $y = x^{9/4} \ln(2x)$ is $x = \sqrt{-2y}$, so that

$$\frac{\mathcal{E}_{\text{crit}}}{\mathcal{E}_m} \approx \frac{2.75}{\Theta_{\text{lc}}^{3/8}} \sqrt{\frac{m_\star}{M_\bullet} \ln \Lambda} \left(\frac{r_m}{r_g} \right)^{3/8}, \quad (61a)$$

$$\ln \mathcal{R}_{\text{lc}}^{-1} \approx -\ln \left[11.0 \Theta_{\text{lc}}^{5/8} \sqrt{\frac{m_\star}{M_\bullet} \ln \Lambda} \left(\frac{r_g}{r_m} \right)^{5/8} \right]. \quad (61b)$$

Equations (57) and (61) are the desired expressions. The predicted values for \dot{N}^{FLC} and \dot{N}^{ELC} are plotted as the curves in Figure 8. The agreement is quite good considering the approximations made; one implication is that the modifications to the Bahcall-Wolf cusp resulting from resonant relaxation have little effect on the total loss rate. The predicted ratios $\dot{N}^{\text{ELC}}/(\dot{N}^{\text{ELC}} + \dot{N}^{\text{FLC}})$ are given in the final column of Table 1; in all cases considered here, the two regimes contribute roughly equally to the total loss rate. We emphasize again that these results apply only to the model considered here, which does not include the contribution of the distributed (stellar) mass to the gravitational potential.

Another interesting property of the steady-state models is the distribution of orbital elements of the captured stars. In the empty-loss-cone regime ($q_{\text{lc}} \ll 1$), loss-cone orbits will have orbital periapsides close to r_{lc} , the physical radius of the loss sphere, but in the full-loss-cone regime ($q_{\text{lc}} \gg 1$), timescales for change in L are comparable with orbital periods and stars at the time of capture can be on orbits with every value of r_p from zero to r_{lc} (Cohn & Kulsrud 1978). One consequence is that stars can experience stronger tidal stresses than if they were all lost from orbits with $r_p = r_{\text{lc}}$ (Guillochon & Ramirez-Ruiz 2013).

Figure 9 shows $d^2F/dr_a dr_p$, the contribution to the loss-cone flux from stars with orbital apoapsides in the range r_a to $r_a + dr_a$ and orbital periapsides in the range r_p to $r_p + dr_p$, for three steady-state models. The details of the calculation are given in the Appendix, which also presents the results of a similar calculation for the classical Bahcall-Wolf solution. As shown there, the computed distribution depends on two quantities: $q_{\text{lc}}(\mathcal{E})$, and $f(\mathcal{E}, \mathcal{R}_{\text{lc}}) \equiv f_{\text{lc}}(\mathcal{E})$. In the Bahcall-Wolf model, unmodified by resonant relaxation, Figure 12 shows that the distribution of orbital elements is a strong function of binding energy. At high \mathcal{E} , i.e. small r_a , $q_{\text{lc}} \ll 1$ and the distribution of periapsides is strongly peaked toward $r_p = r_{\text{lc}}$. At low \mathcal{E} , i.e. large r_a , the loss cone is full and F is nearly independent of r_p .³ After integration with respect to r_a , the distribution of orbital periapsides in the classical Bahcall-Wolf solution has the form shown in the right-hand panel of Figure 12, with a maximum at $r_p = r_{\text{lc}}$ and a very steep drop for $r_p \lesssim r_{\text{lc}}$.

As Figure 9 shows, the inclusion of resonant relaxation modifies this distribution, in the sense of reducing the contribution from stars with $r_p \approx r_{\text{lc}}$. This is an indirect consequence of the strong depletion in f at large binding energies. The depleted orbits are mostly in the empty-loss-cone regime, and their removal implies a larger relative contribution to the loss-cone flux from stars in the full-loss-cone regime, hence $r_p < r_{\text{lc}}$. Figure 9 shows that this modification is severest in the model with the largest r_m , i.e. the largest core; in this model, the distribution of captured stars with respect to r_p is nearly uniform. Even in the model with smallest r_m , i.e. the smallest core, the distribution with respect to r_p is only mildly peaked near r_{lc} , much less so than in the classical solution.

The distributions shown in Figure 9 are computed from models with $m_\star = M_\odot$. Models with larger m_\star have larger q_{lc} , and the distribution of captured stars with respect to periapsis in these models is even more uniform than shown in Figure 9.

To a reasonable approximation, therefore, one can write for all these models:

$$P(< r_p) \approx \frac{r_p}{r_{\text{lc}}}, \quad (62)$$

³ These properties of the orbital distribution were noted previously by Strubbe (2011).

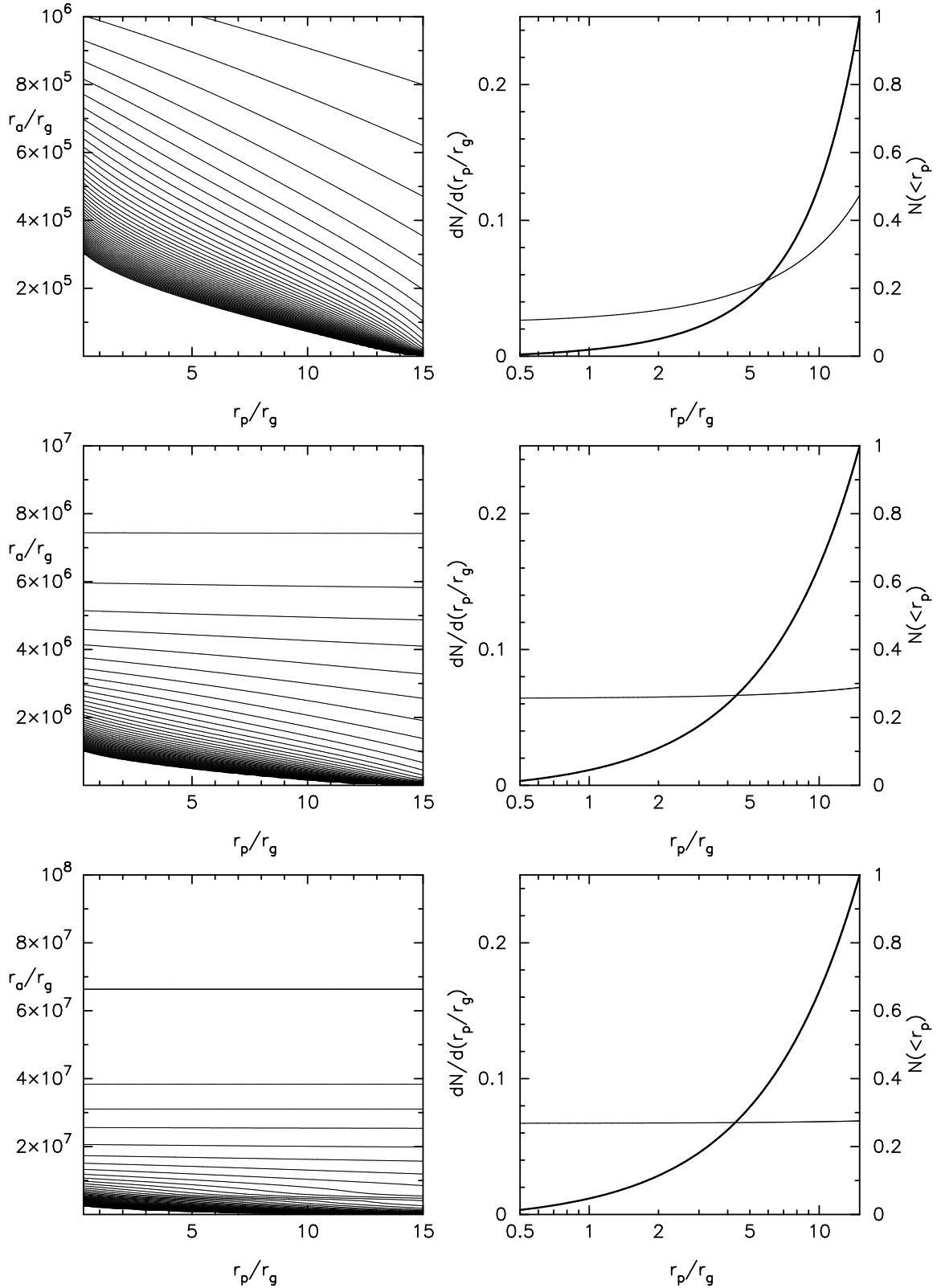


FIG. 9.— Distribution of orbital elements of stars fed to the SBH, computed as described in the Appendix, for the three steady-state models from the right-hand panel of Figure 4. **Left:** Joint distribution of r_a and r_p , equation (A10). Contours are spaced uniformly in $\log F$ and the range in contour values is 10^3 . **Right:** Thin curves show dN/dr_p , obtained by integrating the function in the left panel with respect to r_a at each r_p . Thick curves are the number of stars with periastrides less than r_p , obtained by a second integration with respect to r_p . Both distributions are normalized to unit total number of stars.

where P is the probability of capture from an orbit with periastron less than r_p .

4.2. Time-dependent solutions

In their pioneering work, Cohn & Kulsrud (1978) presented only steady-state solutions. This was in keeping with their parameter choices, which were appropriate to massive black holes at the centers of globular clusters. But energy diffusion timescales near the centers of galaxies are often much longer than in globular clusters, and it is likely that many nuclei have not yet reached steady states under the influence of gravitational encounters. This is presumably the case in all galaxies with parsec-scale cores; but even in galaxies with dense, nuclear star clusters, inferred relaxation times are often of order 10^9 yr or more (Merritt 2009). The nucleus of the Milky Way probably falls in the non-relaxed category (Merritt 2010).

The time-evolution of such nuclei will differ depending on their assumed initial state. One widely discussed model invokes a binary SBH, which scatters and redistributes stars before (presumably) achieving a small enough separation that coalescence of the two black holes can occur (Begelman et al. 1980). The late evolution of such binaries is not well understood, but their initial evolution appears to be fairly robust (Milosavljević & Merritt 2001). After forming a bound pair, at a separation roughly equal to the influence radius of the larger SBH, the binary separation rapidly decreases through the combined influence of dynamical friction and three-body interactions with stars. This phase ends at the so-called “hard binary” separation, $a \approx a_h$, where

$$a_h \equiv \frac{G\mu}{4\sigma^2} = \frac{M_2}{M_{12}} \frac{r_h}{4} \quad (63)$$

(Merritt 2013, equation 8.23). Here, $M_{12} \equiv M_1 + M_2$ is the binary mass; $\mu = M_1 M_2 / M_{12}$; and $r_h \equiv GM_1 / \sigma^2$ is the influence radius of the larger SBH. At separations $\lesssim a_h$, the binary is able to eject stars with high enough velocities that they escape from the nucleus. The binary may “stall” at this radius; or, if a mechanism exists for repopulating the depleted orbits, its semimajor axis can continue to drop.

During the early, rapid phase of its evolution, the binary interacts with stars on orbits having periapses (defined with respect to the binary center of mass) from $\sim r_h$ to $\sim a_h$ or less. This interaction modifies orbits with a range of periapses, from $\sim r_h$ down to $\sim a_h$. Stars on orbits with initial periapses $\lesssim a_h$ are removed entirely from the nucleus. Here, we approximate the stellar distribution at the end of this phase simply as

$$\begin{aligned} f(E, L) &= f_0(E), & L &\gtrsim L_{\text{gap}} \\ &= 0, & L &\lesssim L_{\text{gap}}, \end{aligned} \quad (64)$$

with

$$L_{\text{gap}}(E) = K a_h \sqrt{2[E - \Phi(K a_h)]}, \quad K \approx 1, \quad (65)$$

the angular momentum of an orbit with periapsis at $K a_h$. The corresponding density profile has a core of radius $\sim a$ few $\times a_h$.

Unless the binary mass ratio is close to unity, the core will be small compared with r_h . In this circumstance, one expects post-binary evolution of the stellar distribution to take place on two timescales. Initially, the gap in f at low angular momenta is refilled via diffusion in L . The associated timescale is

$$T_{\text{gap}} \approx \left(\frac{L_{\text{gap}}}{L_c} \right)^2 \mathcal{D}^{-1}(\mathcal{E}_{\text{gap}}) \quad (66)$$

with $\mathcal{E}_{\text{gap}} \approx GM_{\bullet} / a_h$. After a time of $\sim T_{\text{gap}}$, the phase-space density in the region previously emptied by the binary will be approximately constant with respect to L at each E .

On longer timescales, of order $T_{\text{gap}} \lesssim \Delta t \lesssim T_r$, the distribution of orbital energies will evolve, eventually reaching the Bahcall-Wolf steady state.

Evolution of f in the first phase can be approximated by ignoring energy diffusion and writing the Fokker-Planck equation at each energy as

$$\frac{\partial N}{\partial t} \approx \mathcal{D} \frac{\partial}{\partial \mathcal{R}} \left(\mathcal{R} \frac{\partial N}{\partial \mathcal{R}} \right) \quad (67)$$

(Milosavljević & Merritt 2003). By changing variables from \mathcal{R} to $\ell \equiv \sqrt{\mathcal{R}}$, equation (67) becomes the heat conduction equation in cylindrical coordinates with radial variable ℓ and diffusivity \mathcal{D} and has a known solution in terms of basis functions (Merritt 2013, 6.1.5). This solution has been applied to galactic nuclei, assuming for \mathcal{D} the classical angular-momentum diffusion rate, i.e. $\mathcal{D}^{-1} \approx T_r$ (Merritt & Wang 2005).

Initial conditions for the integrations presented here were constructed in the same way as in the previous section, with the added step of setting f to zero at $L \leq L_{\text{gap}}(E)$. Equation (65) is not quite appropriate here given that a_h is defined in terms of σ , the stellar velocity dispersion beyond the SBH influence sphere. Instead, the maximum periapsis of an evacuated orbit was computed from the roughly equivalent expression

$$r_{p,\text{max}} = \frac{\mu}{M_{12}} \frac{r_m}{4} = \frac{q}{(1+q)^2} \frac{r_m}{4} \quad (68)$$

with $q \equiv M_2 / M_1$ the binary mass ratio (Merritt & Szell 2006).

TABLE 2
EVACUATED-CORE MODELS

γ	q	$r_{p,\max}$ (pc)
3/2	0.01	0.005
	0.03	0.014
	0.1	0.041
2	0.01	0.015
	0.03	0.042
	0.1	0.124

Six initial models were constructed: one set with $\gamma = 3/2$ and one set with $\gamma = 2$. These values are, respectively, less than and greater than the Bahcall-Wolf value $\gamma = 7/4$. For each γ , the binary mass ratio in equation (68) was assigned one of the three values

$$q = \{0.01, 0.03, 0.1\} \quad (69)$$

and the initial f was set to zero for orbits with periaapses less than the $r_{p,\max}$ given by equation (68), with $K = 1$. The stellar mass was set to $1M_\odot$, assuming a SBH mass of $4 \times 10^6 M_\odot$, and r_{lc} was set to $15r_g$ as in the previous section. The other important initial parameter was the value of the mass density at large radii. This was set to

$$\rho(r = 1 \text{ pc}) \approx 4.0 \times 10^5 M_\odot \text{pc}^{-3}$$

in the three models with $\gamma = 3/2$, and

$$\rho(r = 1 \text{ pc}) \approx 1.0 \times 10^5 M_\odot \text{pc}^{-3}$$

in the models with $\gamma = 2$. The corresponding values of r_m were approximately 2.0 pc and 6.0 pc, respectively. Table 2 lists the important parameters for the six initial models.

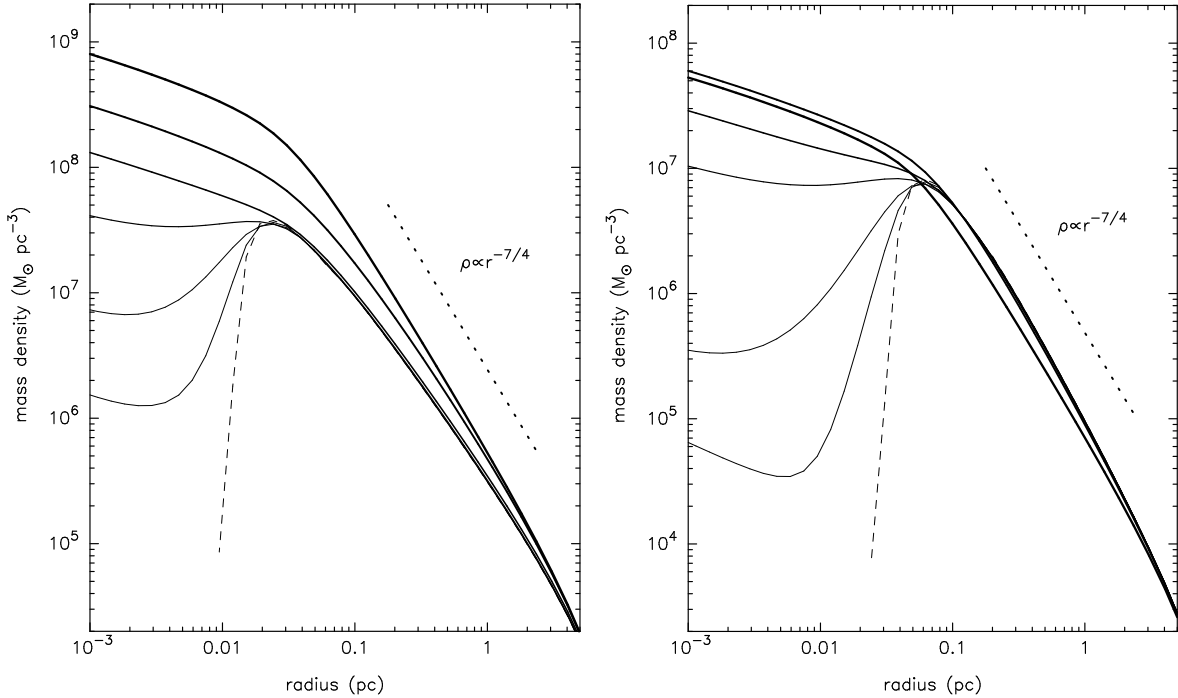


FIG. 10.— Evolution of $\rho(r)$ in two integrations starting from evacuated-core initial conditions, with $q = 0.03$. Left panel: $\gamma = 3/2$; right panel: $\gamma = 2$. The initial density profile is shown as the dashed curve; subsequent times are displayed as curves of increasing width. Displayed times are $\{0.003, 0.01, 0.03, 0.1, 0.5, 10\} \times 10^9$ yr (left panel) and $\{0.01, 0.03, 0.1, 0.2, 0.5, 10\} \times 10^9$ yr (right panel). Scaling assumes $M_\bullet = 4 \times 10^6 M_\odot$. In the right-hand panel, note that the final central density is slightly lower than its value at $t = 5 \times 10^8$ yr.

Figure 10 shows the evolution of the mass density profile in the two integrations with $q = 0.03$. The values of $r_{p,\max}$ were ~ 0.014 pc ($\gamma = 3/2$) and ~ 0.042 pc ($\gamma = 2$). The two evolutionary timescales discussed above are evident. After a time of $\sim 10^8$ yr ($\gamma = 3/2$) or $\sim 3 \times 10^8$ yr ($\gamma = 2$), the initial core is erased; during this time, the density at $r \gg r_{p,\max}$ hardly changes. Over the next $10^9 - 10^{10}$ yr, energy relaxation causes $\rho(r)$ to approach the Bahcall-Wolf form at large radii.

Evolutionary models like these are characterized by an additional dimensionless parameter: the ratio of the initial core size, $\sim r_{p,\max}$, to the size of the core that forms via resonant relaxation, in the manner discussed in the previous section. Adopting the estimate given above, $r_c \approx 0.03r_m$, for the latter core size, the ratio becomes

$$\frac{r_{p,\max}}{r_c} \approx 8 \frac{q}{(1+q)^2}. \quad (70)$$

This ratio is ~ 0.25 for both of the models of Figure 10, implying that the final core should be somewhat larger than the initial core, as seen in the figure. There is however a change in the structure of the core. Initially, the core is formed by the exclusion of orbits with small periaapses, implying a zero configuration-space density below some radius. The core that forms at late times is characterized by a deficit of orbits with high binding energies; as discussed above, the implied density is nonzero, $\rho \sim r^{-1/2}$ near the center, due to orbits with low binding energies and small angular momenta that pass near the center.

The fact that the ratio in equation (70) is less than unity for these models implies that the initial timescale for core refilling is set by resonant, and not classical, relaxation. We can estimate that time from equation (36), replacing a by $r_{p,\max}$. The result is $\sim 6 \times 10^7$ yr ($\gamma = 3/2$) and $\sim 3 \times 10^8$ yr ($\gamma = 2$), quite consistent with the evolution seen in Figure 10.

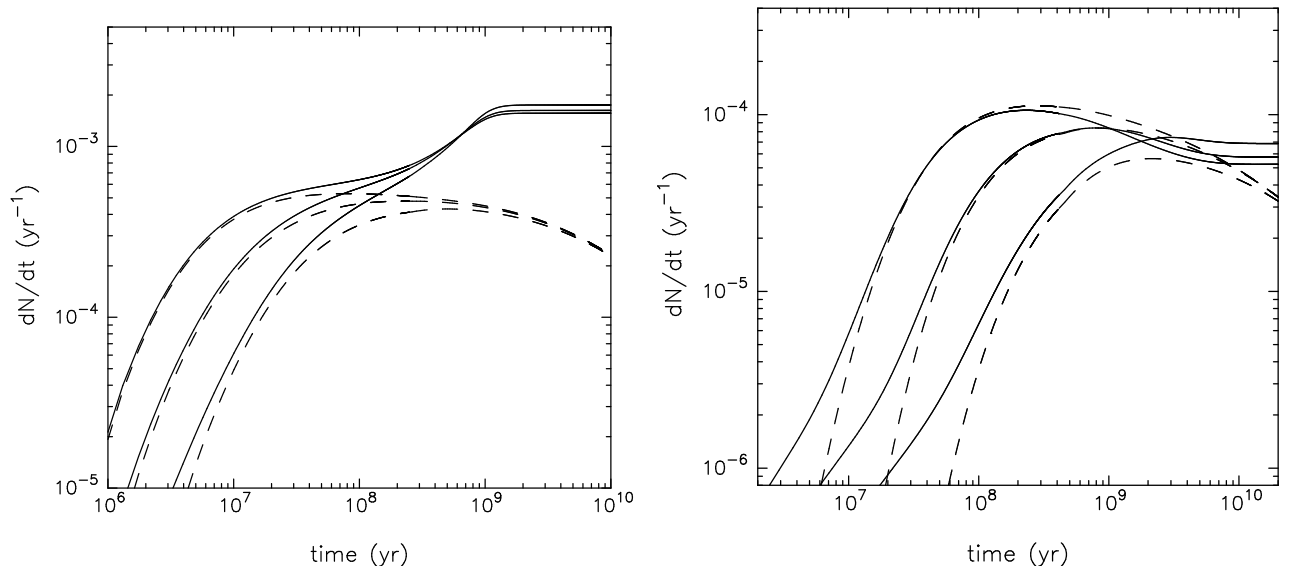


FIG. 11.— Total loss rates for the six models with evacuated cores at $t = 0$. Left: $\gamma = 3/2$; right: $\gamma = 2$. Scaling assumes $M_\bullet = 4 \times 10^6 M_\odot$. Dashed curves are from integrations starting from the same initial conditions, but with the energy diffusion terms artificially set to zero.

The two evolutionary timescales are reflected also in the change with time of the SBH feeding rate \dot{N} . Figure 11 plots this quantity for each of the six models with initially evacuated cores. Also plotted there, as the dashed curves, are the feeding rates from a second set of integrations in which the energy diffusion terms were artificially set to zero. In those models, evolution of f at each E is described approximately by equation (67). Comparison of the two sets of curves shows in a very direct way how the early evolution is determined by angular-momentum diffusion and the late evolution by energy diffusion.

In the models of Figure 11, steady-state loss rates are only achieved after a time of $\sim 10^9$ yr ($\gamma = 3/2$) or $\sim 3 \times 10^9$ yr ($\gamma = 2$). These times are fixed by the classical relaxation time, equation (4), and hence by the adopted density normalization. It is clear from this small set of examples that many nuclei, including that of the Milky Way, might not be in a steady state with regard to SBH feeding rates. Indeed, in nuclei with SBH masses larger than the value assumed here ($4 \times 10^6 M_\odot$), equation (36) implies that even the initial timescale for core refilling due to angular momentum diffusion could exceed 10^{10} yr.

5. DISCUSSION

5.1. Comparisons with earlier work

The consequences of resonant relaxation for the steady-state distribution of stars around a SBH have been discussed by earlier authors (Hopman & Alexander 2006b; Madigan et al. 2011) using more approximate methods. Here we compare the results of those studies with the results obtained here.

Hopman & Alexander (2006b) derived steady-state solutions for $N(E)$ in the fixed gravitational potential of a SBH. Their evolution equation had the form

$$\frac{\partial N}{\partial t} = -\frac{\partial F_{\mathcal{E}}}{\partial \mathcal{E}} - F_{\text{NR}}(\mathcal{E}, t) - \chi \frac{N}{T_{\text{RR}}}. \quad (71)$$

The term F_{NR} accounts for loss of stars into the SBH via “non-resonant,” i.e. classical, diffusion in L ; Hopman & Alexander (2006b) adopted an expression similar to that used by Bahcall & Wolf (1977) in their earlier study of the 1d problem. The last term on the right hand side of equation (71) approximates the loss rate at energy \mathcal{E} due to resonant relaxation; T_{RR} is an estimate of the resonant relaxation time, and the dimensionless factor $\chi = \mathcal{O}(1)$ was included to parametrize uncertainties in the efficiency of resonant relaxation and in the degree of depletion of phase space near the loss-cone boundary; the latter could not be modeled in their study due to the 1d, $f = f(\mathcal{E})$ approximation.

We can cast our Fokker-Planck equation for $f(\mathcal{E}, \mathcal{R}, t)$ in an analogous form, as follows. Equation (10) is

$$\frac{\partial N(\mathcal{E}, \mathcal{R})}{\partial t} = \dots \mathcal{J} \frac{\partial}{\partial \mathcal{R}} \left(D_{\mathcal{R}\mathcal{R}} \frac{\partial f}{\partial \mathcal{R}} + D_{\mathcal{R}} f \right) \quad (72)$$

where terms depending on the energy-space flux have been omitted. Adopting the expressions (13) for the flux coefficients due to RR, equation (72) becomes

$$\frac{\partial N(\mathcal{E}, \mathcal{R})}{\partial t} = \dots 2A(\mathcal{E}) \frac{\partial}{\partial \mathcal{R}} \left[\mathcal{R}(1 - \mathcal{R}) \frac{\partial N}{\partial \mathcal{R}} \right]. \quad (73)$$

Integrating this expression $d\mathcal{R}$ yields an evolutionary equation for $N(\mathcal{E})$:

$$\frac{\partial N(\mathcal{E}, t)}{\partial t} = \dots 2A(\mathcal{E}) \left[\mathcal{R}(1 - \mathcal{R}) \frac{\partial N}{\partial \mathcal{R}} \right]_{\mathcal{R}_{\text{lc}}}^1 \quad (74a)$$

$$= \dots - 2A(\mathcal{E}) \mathcal{R}_{\text{lc}}(\mathcal{E}) [1 - \mathcal{R}_{\text{lc}}(\mathcal{E})] \left(\frac{\partial N}{\partial \mathcal{R}} \right)_{\mathcal{R}_{\text{lc}}}. \quad (74b)$$

To make further progress we need an ansatz for the \mathcal{R} -dependence of N . A natural choice is the “empty-loss-cone” solution (53), which implies

$$N(\mathcal{R}; \mathcal{E}) = N(1; \mathcal{E}) \left(1 - \frac{\ln \mathcal{R}}{\ln \mathcal{R}_{\text{lc}}} \right) = \frac{N(\mathcal{E}) \ln(\mathcal{R}/\mathcal{R}_{\text{lc}})}{\ln \mathcal{R}_{\text{lc}}^{-1} + \mathcal{R}_{\text{lc}} - 1} \quad (75)$$

where we have identified $N(\mathcal{E}) = \int N(\mathcal{R}; \mathcal{E}) d\mathcal{R}$. Inserting (75) into (74b) then yields

$$\frac{\partial N}{\partial t} \approx \dots - \frac{2A(\mathcal{E})N(\mathcal{E})}{\ln(1/\mathcal{R}_{\text{lc}})} \quad (76)$$

and comparing this expression with (71), we conclude

$$\chi \approx 2 \frac{T_{\text{RR}}(\mathcal{E})A(\mathcal{E})}{\ln(1/\mathcal{R}_{\text{lc}})}. \quad (77)$$

Adopting equation (14) for $A(\mathcal{E})$, and Hopman & Alexander (2006b)’s expression for T_{RR} :

$$T_{\text{RR}} \equiv \frac{A_{\text{RR}}}{N_{\star}(< a)} \left(\frac{M_{\bullet}}{m_{\star}} \right)^2 \frac{P^2(a)}{t_{\text{coh}}(a)}, \quad A_{\text{RR}} \approx 3.56 \quad (78)$$

then yields

$$\chi \approx \frac{18}{\ln \mathcal{R}_{\text{lc}}^{-1}}. \quad (79)$$

In the models computed here, equation (61b) gives $\ln \mathcal{R}_{\text{lc}}^{-1} \approx 12$, so that $\chi \approx 1.5$. Hopman & Alexander (2006b) presented steady-state solutions for the cases $\chi = \{1, 3, 10\}$. Their Figure 8 shows steady-state density profiles, $\rho(r)$, for the Milky Way nucleus, assuming $\chi = 1$ and $\chi = 10$; there are depletions with respect to the $\chi = 0$ (classical) case inside radii of ~ 0.05 pc and ~ 0.2 pc, respectively. While Hopman & Alexander (2006b) do not clearly state the density normalization for their models (there are no units on the vertical axis of their Figure 8), the mass density at 1 pc appears to be $\sim 1 \times 10^5 M_{\odot} \text{ pc}^{-3}$, which would place it midway between the two models in Figure 4 with the lower density normalizations. The core sizes in those models are similar to the values found by Hopman & Alexander (2006b).

One issue that complicates a comparison of Hopman & Alexander’s (2006) results with ours is the choice that they made for the coherence time. They defined

$$\frac{1}{t_{\text{coh}}} \equiv \left| \frac{1}{t_{\text{coh},\text{M}}} - \frac{1}{t_{\text{coh},\text{S}}} \right|, \quad (80)$$

with $t_{\text{coh},\text{M}}$ and $t_{\text{coh},\text{S}}$ defined in essentially the same way as here (equation 15). Both quantities are positive by definition, and the minus sign in equation (80) was said to account for the fact that mass precession is retrograde and Schwarzschild precession prograde. At a certain energy / radius, the coherence time as defined by equation (80)

becomes infinite. While the precession rate of a single orbit can be zero (if its eccentricity has precisely the right value), orbits of other stars at similar radii will still precess, implying a finite coherence time at every radius.

A very different approach to the problem was taken by Madigan et al. (2011), who developed an ad-hoc statistical model for the effects of resonant relaxation, calibrated against N -body simulations. Nevertheless, their and our results about the depletion of $f(E)$ at high binding energies and the corresponding flattening of the density profile are qualitatively similar. The size of the steady-state core predicted by Madigan et al. (2011) for the Milky Way was $\lesssim 0.05$ pc, consistent with the core sizes in some of the models shown here in Figure 4.

5.2. Comparison with the distribution of stars at the center of the Milky Way

The distribution of stars near the center of the Milky Way has long been known to depart from the Bahcall-Wolf steady-state form. Solutions of the isotropic Fokker-Planck equation that include the stellar potential suggest that the Bahcall-Wolf solution (which ignores the stellar potential) should be valid out to distances of at least $\sim 0.2 r_m$ from the SBH (Merritt 2013, 7.1.1). Applied to the Milky Way, this result implies that the $n \sim r^{-7/4}$ cusp, if present, would extend outward to $\sim 0.2 - 0.6$ pc. However, number counts of the late-type (i.e. old) stars fail to show a cusp. Instead, the density of these stars (most of which are believed to be red giants) rises only very slowly, if at all, toward the center inside a projected radius of ~ 0.5 pc (Buchholz et al. 2009; Do et al. 2009; Bartko et al. 2010).

Madigan et al. (2011) proposed that resonant relaxation was responsible for the Milky Way core. However the steady-state cores found by those authors were about an order of magnitude smaller than the core observed in the Milky Way. The core sizes in Hopman & Alexander (2006b)’s steady-state models were also substantially smaller than 0.5 pc, as noted above. The arguments presented here (§ 3) suggest that the size of a steady-state core that is produced by the action of resonant relaxation should scale roughly with r_m . Based on the results plotted in Figure 4, a steady-state core as large as ~ 0.5 pc in the Milky Way would require $r_m \gtrsim 20$ pc, far larger than most estimates of the SBH influence radius.

A likely resolution to this apparent discrepancy is to assume that the Milky Way nucleus is not yet in a steady state with regard to diffusion in energy (Merritt 2010). The observed core could then result from a combination of initial conditions, which have not yet been erased by the effects of gravitational encounters; and the depleting effects of resonant relaxation. This possibility is explored in more detail in a separate paper (Merritt et al. 2015).

5.3. Other consequences of the depletion of f at large binding energies

The striking depletion in $N(E)$ at large binding energies found here, and in some earlier studies, is a consequence of two things: (i) the sudden drop in the angular momentum diffusion time below a certain energy, due to resonant relaxation; and (ii) the absence of any mechanism that might maintain a high density of stars near the SBH in spite of the high loss rate. The first assumption seems robust; the second less so, since the forms for the diffusion coefficients adopted here are only likely to be valid beyond a certain distance from the SBH. If diffusion times become long again in the “Schwarzschild,” “Kerr” etc. regions of Figure 1, a high density of stars (or compact objects) might be maintained very near the SBH. Ongoing star formation in this region could also maintain a nonzero f .

Assuming for the moment that neither happens, one can speculate about the consequences of the depletion. An approximate representation of the steady-state phase space density in the models of Figures 4 and 5 is

$$\begin{aligned} f(\mathcal{E}, \mathcal{R}) &\approx \bar{f}(\mathcal{E}), & \mathcal{E} \lesssim \mathcal{E}_{\text{eq}} \\ &\approx 0, & \mathcal{E} \gtrsim \mathcal{E}_{\text{eq}} \end{aligned} \quad (81)$$

with \mathcal{E}_{eq} the binding energy at which resonant relaxation begins to dominate classical relaxation—roughly, the energy of an orbit with radius a_{eq} given by equation (38). Properties of models having the functional form (81) for f have been discussed (Merritt 2010; Antonini & Merritt 2012). The distribution of orbital eccentricities, $N(e)$, approximates a delta function, $N(e) \sim \delta(1 - e)$, for $r \ll a_{\text{eq}}$, since the only orbits that approach closely to the SBH are very eccentric ones.

Figure 4 suggests that in the Milky Way, the region of strong depletion would have a radius < 0.1 pc. As noted above, this is probably too small to explain the observed core; but since the depletion due to resonant relaxation occurs on a $\sim 10^8$ yr timescale, it is likely to be present whatever the explanation for the larger observed core unless the “initial conditions” were extreme.

In the Milky Way, the brightest stars in this region are the S-stars and the stars in the two stellar disks. Their presence is not inconsistent with the depletion discussed here since these stars must have formed very recently: less than $\sim 10^8$ years ago in the case of the S-stars, and less than $\sim 10^7$ years ago in the case of the stellar disks (Schödel 2011).

The evolutionary models presented here are more relevant to old stellar populations. Stellar-mass black holes, with masses $\sim 3M_\odot - 30M_\odot$, are likely to dominate the mass density inside $\sim 10^{-2}$ pc from the Milky Way SBH (Freitag et al. 2006; Hopman & Alexander 2006a), due to mass segregation and due to tidal destruction of normal stars. These are the objects that could become EMRIs, or extreme-mass-ratio inspirals (Sigurdsson & Rees 1997), of great interest to experimental physicists hoping to detect low-frequency gravitational waves. The depletion in f discussed here is likely to have important consequences for the steady-state rate of EMRI production. Exactly what those consequences are can not be stated with certainty yet, since the very eccentric orbits that lead to EMRIs probably evolve in a way that is not well described by the low- L forms of the diffusion coefficients assumed here. Rather, these orbits are subject to “anomalous relaxation,” the qualitatively different way in which orbits evolve when

their precession rate (due to GR) is much higher than that of the field stars (Merritt et al. 2011; Antonini & Merritt 2013).

6. SUMMARY

Integrations of the Fokker-Planck equation describing $f(E, L, t)$, the phase-space density of stars around a super-massive black hole (SBH) at the center of a galaxy, were carried out using a numerical algorithm described in an earlier paper (Merritt 2015). Diffusion coefficients describing both classical and “resonant” relaxation were included. Both steady-state and time-dependent solutions were found. The principal results follow.

1. Steady-state solutions, with fixed density far from the SBH, are similar to the classical, isotropic, Bahcall-Wolf solution, i.e. $f \sim |E|^{1/4}$, $n \sim r^{-7/4}$. However the enhancement of angular momentum diffusion at large binding energies, due to resonant relaxation, implies a depletion in f at those energies and a corresponding density deficit, or “core.” The core radius scales approximately with the gravitational influence radius of the SBH and is a few percent of that radius. The density within the core is $n \sim r^{-1/2}$.

2. Although the inclusion of resonant relaxation has a substantial effect on the density profile near the SBH, the consequences for the SBH feeding rate are much less extreme, since most stars are scattered into the SBH from orbits that lie outside the resonant relaxation regime and since f is strongly depleted in that region. A simple analytic formula is derived, based on the classical diffusion coefficients, that reproduces the numerically-computed loss rates with good accuracy. The depletion in f at large binding energies does significantly affect the distribution of orbital elements of captured stars, in the sense of reducing the contribution from stars on orbits with periapsides $r_p \approx r_{lc}$, the radius of the physical loss sphere.

3. Since energy relaxation times at the centers of galaxies are often very long, time-dependent solutions were also computed. Initial conditions were based on a model in which the SBH was preceded by a massive binary. These models evolve on two timescales: a short timescale during which the core evacuated by the massive binary is refilled via angular-momentum diffusion; and a longer timescale during which diffusion in energy causes the radial distribution of stars to approach the Bahcall-Wolf form far from the SBH.

4. Steady-state cores produced by the effects of resonant relaxation in these models are probably too small to explain the core observed in the distribution of late-type stars at the center of the Milky Way. A possible resolution of the apparent discrepancy would be to assume that the nucleus of the Milky Way has not yet reached a steady state under the influence of gravitational encounters.

5. The depletion in f at large binding energies could have important consequences for the production of EMRIs, or extreme-mass-ratio inspirals. A final decision on this question must await a more careful treatment that includes the effects of “anomalous relaxation,” the qualitatively different way in which eccentric orbits evolve in the post-Newtonian regime.

This work was supported by the National Science Foundation under grant no. AST 1211602 and by the National Aeronautics and Space Administration under grant no. NNX13AG92G.

APPENDIX

DISTRIBUTION OF PERIAPSIDES

In the Cohn-Kulsrud boundary layer treatment, at the moment of capture by the SBH, stars can be on orbits with periapsides in the range $0 \leq r_p \leq r_{lc}$.⁴ The distribution of orbital integrals (\mathcal{E} , \mathcal{R}) of captured stars is given by equation (6.57) of Merritt (2013) (hereinafter DEGN). Here we recast that equation in terms of orbital elements, including the periapsis distance r_p , and use the result to compute the periapsis distribution for stars in a classical Bahcall-Wolf cusp. The same algorithm was used to compute the periapsis distribution for the Fokker-Planck models in § 4.1 (Figure 9).

Differentiating equation (6.57) of DEGN with respect to \mathcal{R} yields the contribution to the loss cone flux from stars in the energy interval \mathcal{E} to $\mathcal{E} + d\mathcal{E}$ and angular momentum interval \mathcal{R} to $\mathcal{R} + d\mathcal{R}$:

$$\frac{d^2 F}{d\mathcal{E} d\mathcal{R}} = 4\pi^2 L_c^2(\mathcal{E}) f(\mathcal{E}, \mathcal{R}, \tau = 1), \quad \mathcal{R} \leq \mathcal{R}_{lc}(\mathcal{E}). \quad (\text{A1})$$

In equation (A1), the phase space density f is understood to be a function of position along an orbit, for any orbit having periapsis inside r_{lc} (Cohn & Kulsrud 1978). The dimensionless variable τ measures position along such an orbit; as τ varies from 0 to 1, r increases from periapsis ($r = r_p$, $f = 0$), to apoapsis ($r = r_a$) and back to r_p again (where f has its maximum value along the orbit). The quantity $f(\mathcal{E}, \mathcal{R}, \tau = 1)$ is expressible in series form as

$$f(\mathcal{E}, \mathcal{R}, 1) = f(\mathcal{E}, \mathcal{R}_{lc}) \left[1 - \frac{2}{\sqrt{y_{lc}}} \sum_{m=1}^{\infty} \frac{e^{-\beta_m^2/4}}{\beta_m} \frac{J_0(\beta_m \sqrt{y})}{J_1(\beta_m \sqrt{y_{lc}})} \right] \quad (\text{A2})$$

(DEGN, equation 6.54). In equation (A2), y is a dimensionless angular momentum variable defined as

$$y \equiv \frac{\mathcal{R}}{P(\mathcal{E})\mathcal{D}(\mathcal{E})}, \quad y_{lc} \equiv \frac{\mathcal{R}_{lc}}{P(\mathcal{E})\mathcal{D}(\mathcal{E})}; \quad (\text{A3})$$

⁴ The calculation described here is non-relativistic and no special consideration is given to stars that travel near or inside the hole’s event horizon, $r \lesssim r_g$.

J_0 and J_1 are Bessel functions of the first kind, and the β_m yield successive zeros of the equation

$$J_0(\beta\sqrt{y_{lc}}) = 0. \quad (\text{A4})$$

In terms of $\alpha_m \equiv \beta_m\sqrt{y_{lc}}$ and $x \equiv \sqrt{y_{lc}}$, equation (A2) is

$$f(\mathcal{E}, \mathcal{R}, 1) = f_{lc}(\mathcal{E})W(q_{lc}, x), \quad (\text{A5a})$$

$$W(q_{lc}, x) = 1 - 2 \sum_{m=1}^{\infty} \frac{e^{-\alpha_m^2 q_{lc}/4} J_0(\alpha_m x)}{\alpha_m J_1(\alpha_m)} \quad (\text{A5b})$$

where $q_{lc} = q_{lc}(\mathcal{E}) = y_{lc}^{-1}(\mathcal{E})$ is defined as in equation (20) and $f_{lc}(\mathcal{E}) \equiv f[\mathcal{E}, \mathcal{R}_{lc}(\mathcal{E})]$.

In the Kepler potential assumed here, $L_c^2(\mathcal{E}) = G^2 M_\bullet^2 / (2\mathcal{E})$ so that

$$\frac{d^2 F}{d\mathcal{E} d\mathcal{R}} = 2\pi^2 (GM_\bullet)^2 \mathcal{E}^{-1} f_{lc}(\mathcal{E}) W(q_{lc}, x). \quad (\text{A6})$$

This can be converted into a distribution in (r_a, r_p) using

$$r_a = a(1+e) = \frac{GM_\bullet}{2\mathcal{E}} (1 + \sqrt{1-\mathcal{R}}), \quad r_p = a(1-e) = \frac{GM_\bullet}{2\mathcal{E}} (1 - \sqrt{1-\mathcal{R}}) \quad (\text{A7})$$

i.e.

$$\mathcal{E} = \frac{GM_\bullet}{r_a + r_p}, \quad \mathcal{R} = \frac{4r_a r_p}{(r_a + r_p)^2}. \quad (\text{A8})$$

The Jacobian is

$$\frac{\partial(\mathcal{E}, \mathcal{R})}{\partial(r_a, r_p)} = \frac{4\mathcal{E}^3}{G^2 M_\bullet^2} \sqrt{1-\mathcal{R}} = 4GM_\bullet \frac{r_a - r_p}{(r_a + r_p)^4} \quad (\text{A9})$$

so that

$$\frac{d^2 F}{dr_a dr_p} = 8\pi^2 G^2 M_\bullet^2 \frac{(r_a - r_p)}{(r_a + r_p)^3} f_{lc}(\mathcal{E}) W(q_{lc}, x). \quad (\text{A10})$$

The quantity $x = x(\mathcal{E}, \mathcal{R}) = \sqrt{\mathcal{R}/\mathcal{R}_{lc}(\mathcal{E})}$ that appears in these expressions can be written in terms of the orbital elements as

$$x = \sqrt{\frac{r_a r_p}{r_{lc}(r_a + r_p - r_{lc})}}. \quad (\text{A11})$$

In the limit of nearly-unbound orbits, i.e. $\mathcal{E} \approx 0$, $x \approx \sqrt{r_p/r_{lc}}$.

These relations can be applied to a classical Bahcall-Wolf cusp. The function $q_{lc}(\mathcal{E})$ follows from equations (9), (20), (26) and (33):

$$q_{lc}(\mathcal{E}) = 8f_0\sqrt{2}\pi^3 \ln \Lambda \mathcal{R}_{lc}^{-1}(\mathcal{E}) (GM_\bullet)^{1/4} Gm_\star r_m^{-5/4} \mathcal{E}^{-5/4}, \quad f_0 \approx 0.036. \quad (\text{A12})$$

We relate $f_{lc}(\mathcal{E})$ to $\bar{f}(\mathcal{E})$ using equations (6.61) and (6.63) of DEGN:

$$f_{lc}(\mathcal{E}) \approx \frac{\bar{f}(\mathcal{E})}{1 + q_{lc}^{-1} \xi(q_{lc}) \ln(1/\mathcal{R}_{lc})} \quad (\text{A13})$$

and identify \bar{f} with equation (26). The results are shown in Figure 12, for a nucleus with $r_m = 10^7 r_g$, $m_\star = M_\bullet / (4 \times 10^6 M_\odot)$, $\ln \Lambda = 15$, and $r_{lc}/r_g = 15$. The computation included 5000 terms in the Bessel series and used a (500×500) grid in (r_a, r_p) . The distribution with respect to r_p can be seen to become nearly uniform for large r_a (full loss cone), while for small r_a (empty loss cone), the distribution is very strongly peaked toward $r_p = r_{lc}$. Roughly 1/2 of all captured stars have periapsides in the range $10r_g \leq r_p < 15r_g (= r_{lc})$ (right panel).

REFERENCES

- Antonini, F., & Merritt, D. 2012, ApJ, 745, 83
 Antonini, F., & Merritt, D. 2013, ApJ, 763, LL10
 Bahcall, J. N., & Wolf, S. 1976, ApJ, 209, 214
 Bahcall, J. N., & Wolf, R. A. 1977, ApJ, 216, 883
 Bartko, H., et al. 2010, ApJ, 708, 834
 Begelman, M. C., Blandford, R. D., & Rees, M. J. 1980, Nature, 287, 307
 Buchholz, R. M., Schödel, R., & Eckart, A. 2009, A&A, 499, 483
 Chandrasekhar, S. 1942, The Principles of Stellar Dynamics. Chicago, The University of Chicago Press.
 Chatzopoulos, S., Fritz, T. K., Gerhard, O., et al. 2015, MNRAS, 447, 952
 Cohn, H. & Kulsrud, R. 1978, ApJ, 226, 1087
 Do, T., Ghez, A. M., Morris, M. R., Lu, J. R., Matthews, K., Yelda, S., & Larkin, J. 2009, ApJ, 703, 1323
 Do, T., Martinez, G. D., Yelda, S., et al. 2013, ApJ, 779, L6
 Freitag, M., Amaro-Seoane, P., & Kalogera, V. 2006, ApJ, 649, 91

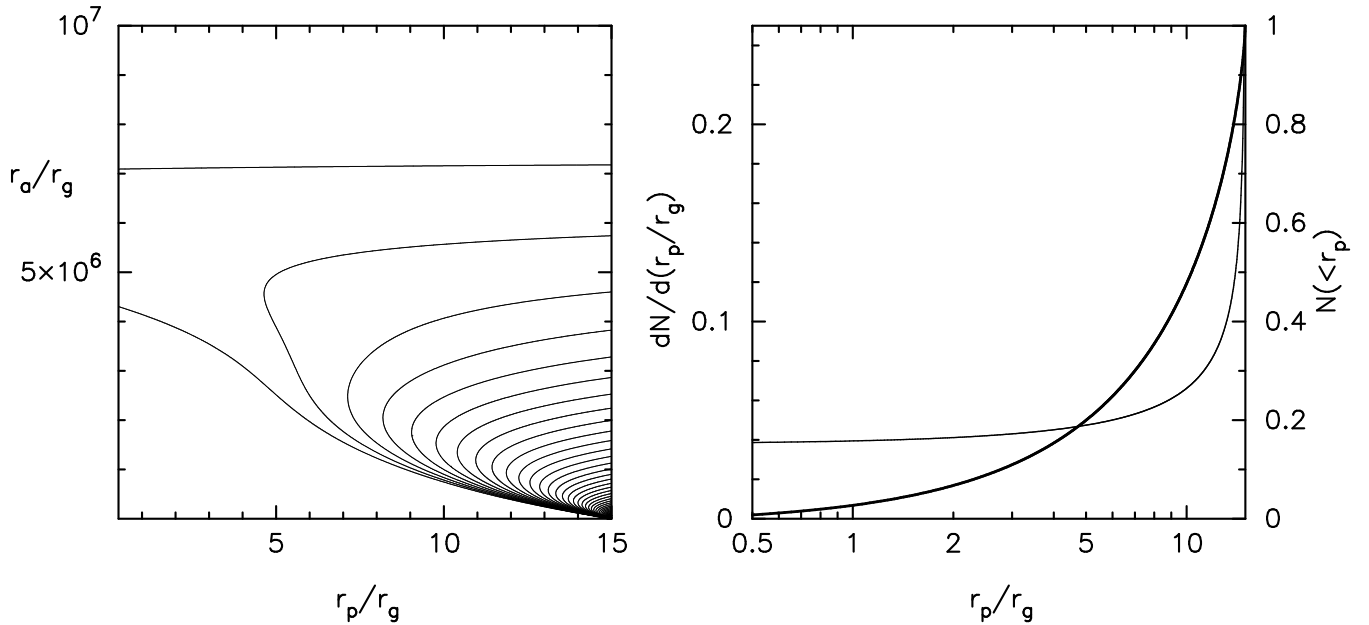


FIG. 12.— Distribution of orbital elements of stars fed to the SBH in a classical Bahcall-Wolf cusp, according to the Cohn-Kulsrud boundary-layer solution. Parameters were $r_m = 10^7 r_g$, $m_* = M_\bullet / (4 \times 10^6 M_\odot)$, $\ln \Lambda = 15$, $r_{lc}/r_g = 15$. **Left:** Joint distribution of r_a and r_p , equation (A10). Contours are spaced uniformly in $\log F$ and the range in contour values is 10^3 . **Right:** Thin curve shows dN/dr_p , obtained by integrating the function in the left panel with respect to r_a at each r_p . Thick curve is the number of stars with periastrides less than r_p , obtained by a second integration with respect to r_p . Both curves are normalized assuming a unit total number of stars.

Guillochon, J., & Ramirez-Ruiz, E. 2013, ApJ, 767, 25
 Hamers, A., Portegies Zwart, S. & Merritt, D. 2014, MNRAS, 443, 355
 Hénon, M. 1961, Annales d’Astrophysique, 24, 369
 Hopman, C. 2009, Classical and Quantum Gravity, 26, 094028
 Hopman, C., & Alexander, T. 2006a, ApJ, 645, L133
 Hopman, C., & Alexander, T. 2006b, ApJ, 645, 1152
 Lee, E. P. 1969, ApJ, 155, 687
 Madigan, A.-M., Hopman, C., & Levin, Y. 2011, ApJ, 738, 99
 Magorrian, J. & Tremaine, S. 1998, MNRAS, 309, 447.
 Merritt, D. 2009, ApJ, 694, 959
 Merritt, D. 2010, ApJ, 718, 739
 Merritt, D. 2013, Dynamics and Evolution of Galactic Nuclei (Princeton: Princeton University Press).
 Merritt, D. 2015, ApJ, 804, 52
 Merritt, D., Alexander, T., Mikkola, S., & Will, C. M. 2010, Phys. Rev. D, 81, 062002
 Merritt, D., Alexander, T., Mikkola, S., & Will, C. M. 2011, Phys. Rev. D, 84, 044024

Merritt, D., Antonini, F., & Vasiliev, E. 2015, submitted to *The Astrophysical Journal*
 Merritt, D., Storchi-Bergmann, T., Robinson, A., et al. 2006, MNRAS, 367, 1746
 Merritt, D., & Szell, A. 2006, ApJ, 648, 890
 Merritt, D., & Wang, J. 2005, ApJ, 621, L101
 Milosavljević, M., & Merritt, D. 2001, ApJ, 563, 34
 Milosavljević, M., & Merritt, D. 2003, ApJ, 596, 860
 Merritt, D., & Vasiliev, E. 2012, Phys. Rev. D, 86, 102002
 Rauch, K. P., & Tremaine, S. 1996, New Astron., 1, 149
 Rosenbluth, M. N., MacDonald, W. M., & Judd, D. L. 1957, Physical Review, 107, 1
 Schödel, R. 2011, Highlights of Spanish Astrophysics VI, 36
 Schödel, R., Merritt, D., & Eckart, A. 2009, A&A, 502, 91
 Sigurdsson, S., & Rees, M. J. 1997, MNRAS, 284, 318
 Strubbe, L. E. 2011, Ph.D. Thesis, University of California, Berkeley